Dense Water Production in Storfjorden, Svalbard, From a 1-Year Time Series of Observations and a Simple Model: Are Polynyas in a Warming Arctic Exporting Heat to the Deep Ocean?

Frédéric Vivier[1] , Antonio Lourenço[1], Ragnheid Skogseth[2], Ilona Goszczko[3], Elisabeth Michel[4] , Clément Rousset[1], Pascale Bouruet-Aubertot[1], Yannis Cuypers[1], Bruno Lansard[4] , and Claire Waelbroeck[1]

[1]LOCEAN-IPSL, CNRS, Sorbonne Université, Paris, France, [2]The University Centre in Svalbard, Longyearbyen, Norway, [3]Institute of Oceanology, Polish Academy of Sciences, Sopot, Poland, [4]LSCE, CEA-CNRS-UVSQ, Université Paris-Saclay—IPSL, Gif sur Yvette, France

Abstract   The formation of dense Brine-enriched Shelf Water (BSW) in Storfjorden is analyzed during Winter 2016–2017 from mooring observations, a polynya model nudged to satellite observations, and an original BSW production model. The ice season was two months shorter than average, yet 44.2 km^3 of sea ice were formed, in line with estimates for the period preceding the atlantification of the Barents Sea in the mid-2000s: A thinner, more fragile ice may favor polynya openings and frazil ice production. A saline specimen of BSW was produced in large volumes, corresponding to an annual mean transport of 0.042 Sv, larger than previous estimates. The important production is due to the preconditioning of the polynya with a more saline source water, exceeding the pre-2005 values by 0.37. The BSW overflow was observed on the West Spitsbergen shelf slope from hydrographic sections down to 750 m, thus entering the Norwegian Sea Deep Water layer. Its core temperature was about 1℃ warmer than the pre-2005 values owing to the entrainment of a warmer water in Storfjordrenna, suggesting that a part of the excess surface heat of the Barents Sea could be exported into the deep ocean. Overall our results suggest that dense water formation in the Storfjorden polynya may not, at least for now, be hampered by the atlantification of the Barents Sea, and perhaps even temporarily favored by the more saline source water. Anomalous atmospheric warming during the Winter-Spring may however disrupt the production, as was observed 1 year before.

Plain Language Summary   Sea-ice extent has strongly declined in the Barents Sea since the mid-2000s. The sea has also become warmer and saltier, a phenomenon referred to as atlantification. This raises concerns regarding the future of dense water production in coastal polynyas, an essential cog in the climate machine. Polynyas work as ice factories, releasing large quantities of salt in the ocean, which can lead surface waters to cascade into the deep ocean when dense enough. We analyze dense water production in Winter 2016–2017 in the Storfjorden polynya (Svalbard) from a time series of hydrographic observations and an ice production model. Despite a shorter freezing season, the ice production and salt release remained average, while preconditioning with a more saline source water permitted the production of a particularly saline dense water in large volumes. The dense bottom plume was observed to sink into the deep ocean. It was warmer than in the past, suggesting that part of the excess surface heat could be stored at depth. Overall our results suggest that dense water production may not, at least for now, be hampered by the atlantification of the Barents Sea, unless strongly anomalous winter atmospheric warming disrupts ice production, as observed 1 year before.

1. Introduction

Polynyas occupy a small fraction of the cryosphere, yet they play an important role in the Earth's climate. Over the Arctic Ocean shelves, their large ice production and associated brine rejection forms dense water that contributes to maintain the cold halocline layer in the Arctic Ocean, shielding the sea ice from the warm Atlantic Water (AW) (Aagaard et al., 1981; Cavalieri & Martin, 1994; Morales Maqueda et al., 2004; Winsor & Björk, 2000). If dense enough the Brine-enriched Shelf Water (BSW) can ventilate the intermediate and deep layers of the Arctic Ocean (Aagaard, 1981; Aagaard et al., 1985; Rudels, 1986; Rudels & Quadfasel, 1991; Swift et al., 1983). Dense plumes of BSW were observed to spread on the shelf of Novaya Zemlya and Svalbard bank (Midttun, 1985). In 1986 a

Resources: Frédéric Vivier,
Ilona Goszczko
Software: Frédéric Vivier
Supervision: Frédéric Vivier
Visualization: Frédéric Vivier
Writing – original draft: Frédéric Vivier
Writing – review & editing:
Antonio Lourenço, Ragnheid Skogseth,
Ilona Goszczko, Elisabeth Michel,
Clément Rousset, Pascale Bouruet-
Aubertot, Yannis Cuypers, Bruno Lansard,
Claire Waelbroeck

remarkable gravity-driven plume originating from Storfjorden was traced on the continental slope of Svalbard down to depths of more than 2,000 m in Fram Strait (Quadfasel et al., 1988). This observation, jointly with the concurrent sampling of a particularly saline BSW (>35.4) in Storfjorden (Anderson et al., 1988), attracted much attention to the Storfjorden polynya, fostering an abundant subsequent research initiated by a dedicated survey with current meter moorings (Schauer, 1995) and numerical modeling of the plume dynamics (Jungclaus et al., 1995).

Storfjorden is a large (~190 km long) and deep (~190 m) bay to the south-east of the Svalbard Archipelago (Figure 1), hosting to its northeastern part a recurrent latent heat polynya in winter that opens with northeasterly winds (Haarpaintner, 1999; Haarpaintner, Gascard, & Haugan, 2001; Schauer, 1995; Skogseth, Fer, & Haugan, 2005). Storfjorden is bordered by the islands of Spitsbergen, Barentsøya and Edgeøya to the north, separated by the shallow straits of Heleysundet and Freemansundet, respectively, in which strong tidal currents are reported (Skogseth et al., 2008, 2013). To the south, the mouth to the Barents Sea is barred by a 120-m deep sill at 77°N. South of this sill, Storfjordrenna, a trough bordered by the shallow banks of Storfjordbanken, Hopenbanken, and Svalbardbanken (also known as Spitsbergen Bank) stretches out to the continental slope of western Svalbard. Storfjordrenna also marks the boundary between water originating from the Arctic and water of subtropical origin carried by a branch of the West Spitsbergen Current flowing cyclonically guided by topography (e.g., Loeng, 1991). The Polar Front (PF), that separates Arctic from Atlantic domain, is thus close to the mouth of Storfjorden.

The primary source of the local BSW formation in Storfjorden is the considerable volume of ice, of order 30 to 50 km³, produced each year in the polynya, releasing about 1 gigaton of salt in the ocean (e.g., Jardon et al., 2014; Skogseth et al., 2004). The Storfjorden polynya thus accounts for only 4% of the total ice production of major Arctic polynyas (1178 ± 65 km³; Iwamoto et al., 2014), but it is one of the best-sampled polynyas in the Arctic, from which much can be learned about the polynya processes in general. The seasonal cycle of BSW formation can be schematized as follows (Skogseth, Fer, & Haugan, 2005). After the onset of freezing, the BSW produced by brine rejection gradually fills the depressions of the fjord up to the sill level before spilling into Storfjordrenna. This overflow strengthens up to March and remains constant through April and May, maintained by the transformation of inflow waters into BSW. The overflow gradually weakens in summer, before reaching an occasional discharge regime toward October. The flow of BSW was estimated at the sill from 3 years (2004–2006) of moored Acoustic Doppler Current Profiler (ADCP) data by Geyer et al. (2009) yielding an annual mean transport of 0.03 Sv (1 Sv ≡ 10⁶ m³ s⁻¹). This value is consistent with estimates of 0.03–0.04 Sv and an average annual BSW production of 1,030 km³ for the period 1998–2002 stemming from a polynya model and salt budgets in the basin (Skogseth et al., 2004). These estimates are somewhat smaller than the 1,600 km³ and 0.05 Sv initially computed by Schauer (1995) from a pair of current meter moorings located 30 km south of the sill, with thus an additional possible contribution from entrained water. The flow of BSW continues as a dense bottom plume along the northern slope of Storfjordrenna (e.g., Fer et al., 2003; Schauer, 1995). Its ultimate fate, that is, whether it sinks along the continental slope into the deep ocean, as observed in 1986, 1988, and 2002 (Akimova et al., 2011), or inserts in ambient waters at shallower depth depends on its density, that is mostly on the salinity of the BSW forming in Storfjorden. The latter varies substantially from 1 year to the next, ranging from 34.8 (the threshold defining BSW) to a record 35.83 (Anderson et al., 2004; Skogseth, Fer, & Haugan, 2005). The factors governing this variability are plural, including the volume of ice forming in the polynya and the preconditioning, that is, the salinity of the source water (primarily Arctic Water) being transformed (Jardon et al., 2014; Schauer, 1995; Skogseth et al., 2004).

Most of the knowledge about the BSW production in Storfjorden stems from hydrographic observations collected prior to 2005, which appears as a hinge year in the northern Barents Sea. Indeed, although the Barents Sea ice has been declining with increased Atlantic heat transport since the 1980s (Årthun et al., 2012), a sharp increase in temperature and salinity together with reduced sea-ice cover is only apparent from the mid-2000s in the northern Barents Sea (e.g., Barton et al., 2018; Lind et al., 2018; Onarheim & Årthun, 2017). In July 2016 an exhaustive hydrographic survey was conducted in Storfjorden revealing an unusual situation, the most salient aspects of which were the absence of a gravity driven overflow of BSW south of the sill, with only remnants of relatively fresh BSW (maximum salinity of 34.95) found in the depression of Storfjorden, as well as a large intrusion of Modified Atlantic Water (MAW) far north inside Storfjorden, which was previously unreported (Vivier et al., 2023). This survey occurred in the wake of particularly mild winter with the lowest sea-ice cover of the
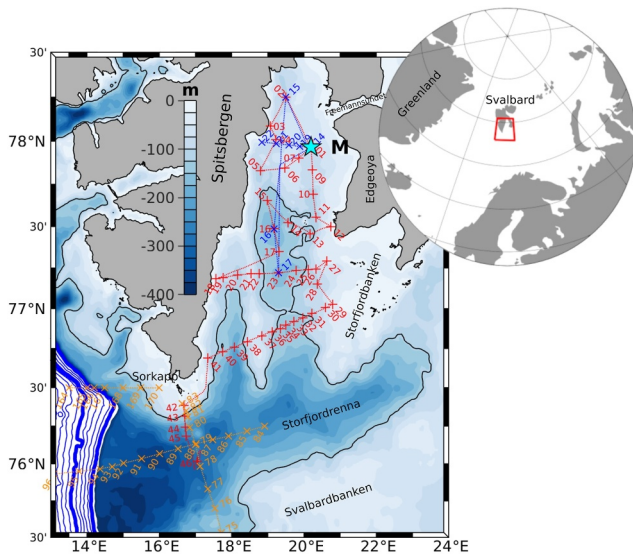
Figure 1. Bathymetric map of Storfjorden and location of the two moorings located a few hundred meters apart (star). Hydrographic stations occupied during the STEP deployment cruise (July 2016) are shown in red, those of the recovery cruise (September 2017) in blue, and those for the IOPAN AREX survey (July 2017) in orange. The 120 m isobath that marks the sill at the entrance of Storfjorden is indicated (black contour). Bold blue lines on the shelf break and slope are the 500 and 1,000 m isobaths.

Barents Sea over the entire satellite record. Given the long-term changes occurring in the Barents Sea, these observations raised the question as to whether the highly unusual hydrographic state of Storfjorden in the summer 2016 was a prefiguration of more permanent changes.

A mooring recording hydrography and currents was deployed during the July 2016 cruise and recovered 14 months later, thus covering a complete BSW production cycle. The purpose of this paper is to document the polynya activity and BSW production from the analysis of mooring observations. The data set is completed with hydrographic profiles collected in Storfjorden during the September 2017 recovery cruise, but also conductivity-temperature-depth (CTD) stations occupied in July 2017 in Storfjordrenna and on the west Spitsbergen margin as part of the Polish AREX (ARctic EXperiment) survey. The ice production and salt release in 2016–2017 is estimated from the polynya model of Jardon et al. (2014) nudged to satellite sea-ice concentration (SIC) data, whereas an original model is developed to estimate the volume of BSW formed based on mooring data and salt forcing.

This paper is organized as follows. We first introduce the in situ data set and ancillary data (satellite observations and atmospheric forcing). The ice production model is succinctly described in Section 2.3 whereas Section 2.4 presents the new box model developed to estimate BSW production. The evolution of water masses in Storfjorden and Storfjordrenna is analyzed in Section 3.1 followed by the estimation of the ice production during the winter 2016–2017 and of the associated volume of BSW in Sections 3.3 and 3.4, respectively. Results are discussed in Section 4, followed by a summary of the main results and concluding remarks.

2. Data and Methods

2.1. In Situ Data

2.1.1. Moorings

Two moorings, hereinafter referred to as M1 and M2, were deployed in Storfjorden on 14 July 2016 from R/V *L'Atalante* and were recovered on 28 September 2017 from R/V *Pourquoi-Pas?* (STEP-2016 and STEP-2017 cruises). The two moorings were deployed a few hundred meters apart at a water depth of 99 m at 77°58′N and 20°12′E (Figures 1 and 2), in the center of the region occupied by the polynya during winter (Haarpaintner, 1999; Skogseth et al., 2004).

Mooring M1 was composed of six Seabird SBE-37 MicroCAT CTD recorders regularly spaced throughout the water column between 15 and 90 m, that all returned 441 days of data (Table 1). Their accuracy was $\pm0.002\,°C$ for temperature and ±0.003 mS/cm for conductivity. All instruments were calibrated by the manufacturer in 2018 except for the one at 15 and 75 m. Based on pre- and post-campaign calibration, a linear drift correction for conductivity and temperature was applied. The correction ranged between 0 and -0.007 for salinity and 0 and $7 \times 10^{-4}\,°C$ for temperature. A significant bias correction of -0.02 was applied to the salinity data from the SBE-37 at 75 m (the latter was not calibrated after the campaign). This correction was determined by comparing the density of the different instruments during several episodes in November-December 2016, each lasting a few days, where the water column was almost perfectly homogeneous. During these episodes, potential density at all depths agreed to within 3×10^{-3} kg m^{-3} except at 75 m. The salinity correction at 75 m restored the stability of the water column. Finally a manual editing was performed to flag nonphysical salinity data from the different instruments. To refine vertical temperature profiles, the mooring was also equipped with 16 autonomous temperature sensors (RBR solo or duet models; $\pm0.002\,°C$ accuracy; Table 1). The time drift for each instrument was linearly corrected. Six RBRs were located at the same depth as SBE-37, which made it possible to compare their temperature measurements. Between January and May 2017 the temperature was extremely stable, close to the freezing point. The two data sets agree to within $2 \times 10^{-3}\,°C$ during this period. Mooring M1 was also designed to measure currents. An upward looking ADCP operating at 300 kHz (Workhorse Sentinel from Teledyne RD
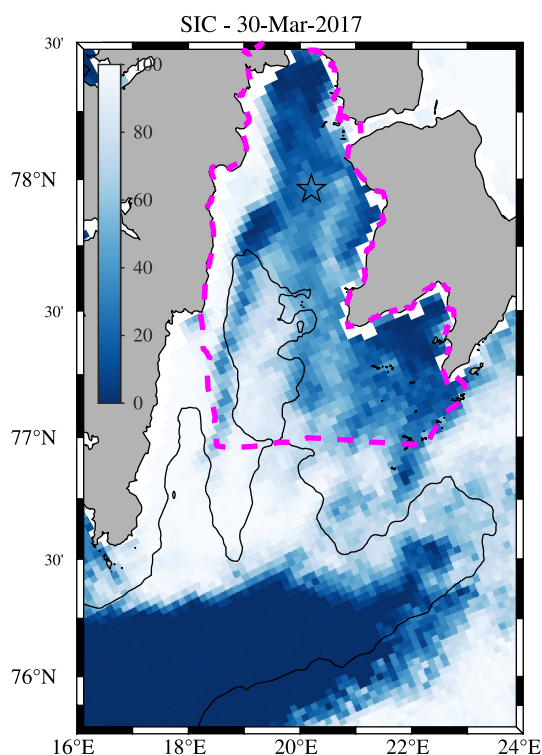
Figure 2. Sea-ice concentration on 30 March 2017 from the 3.125 km resolution Advanced Microwave Scanning Radiometer 2 satellite product from Bremen University. The thin black line denotes the 120 m isobath that marks the sill at the entrance of Storfjorden and the mooring location is indicated by a black star. The magenta dashed line encloses the domain over which ice production is computed with the polynya model.

Instruments) was installed at a depth of 87 m. It recorded the three components of the velocity every 100 min over twenty 4-m-thick vertical cells which centers ranged between 5 and 81 m. A single point Doppler current meter (Aquadopp model from Nortek) recorded the current closer to the bottom (90 m) every 20 min. While the ADCP includes a temperature sensor, the water salinity is instead fixed at 35 for sound speed calculation by the instrument; given the actual range of salinity variations, this approximation induces a velocity error of less than 3%.

The shorter M2 mooring, primarily dedicated to biogeochemistry, included only 3 sensors for hydrography (Table 1): two RBRs and one Seabird SBE-63 + SBE-37 CTD-O_2 recorder at 73 m, measuring temperature, salinity, pressure and dissolved O_2 concentration every hour. A linear time drift correction was applied to each instrument. Based on pre- and post-campaign calibration, a linear drift correction for conductivity corresponding to a salinity ranging between −0.001 and −0.003 was also applied. The temperature sensor did not drift. Dissolved oxygen concentration data from the SBE-63 recorder were compared with the O_2 profile taken at the time of deployment. The latter profile, which was carefully calibrated with ex situ Winkler titrations (accuracy of 2 μmol kg^{-1}), was stable at 350 μmol kg^{-1} between 70 and 80 m, while the corresponding SBE-63 value was 334 μmol kg^{-1}. A 16 μmol kg^{-1} bias correction was therefore added to the time series.

2.1.2. CTD Profiles

During the July 2016 deployment cruise a network of 46 hydrographic stations was occupied on different sections across Storfjorden and Storfjordrenna (Vivier et al., 2023), while only nine stations were occupied on 28–29 September 2017 during the shorter recovery cruise (Figure 1). All hydrographic profiles were collected with a Seabird SBE911plus CTD probe with an accuracy of ±0.001°C for temperature and ±0.003 mS/cm for conductivity.

Additionally, to track the dense plume overflowing from Storfjorden, we have examined a series of 29 hydrographic profiles along three sections in Storfjordrenna and across the south-western shelf of Spitsbergen (Figure 1) collected by the Institute of Oceanology, Polish Academy of Sciences (IOPAN) between 30 June and 15 July 2017 from R/V *Oceania* using a Seabird SBE911plus CTD. These observations were collected in the frame of the long-term monitoring program AREX (Walczowski et al., 2017).

In subsequent analyses of hydrographic data we have used the Gibbs Sea Water toolbox implementing the Thermodynamic Equations of Sea Water 2010 (TEOS-10) (McDougall & Barker, 2011). However, we shall present practical salinity and potential temperature rather than absolute salinity and conservative temperature for the sake of comparison with existing literature.

2.2. Atmospheric and Sea-Ice Concentration Data

Hourly surface atmospheric parameters, including air temperature, relative humidity, pressure, wind speed and direction, net turbulent (latent and sensible) and radiative (shortwave and longwave) heat fluxes were obtained from the European Center for Medium-Range Weather Forecasts (ECMWF) Reanalysis (ERA5) at a 30 km spatial resolution (Hersbach et al., 2020). ERA5 is produced by the Copernicus Climate Change Service (C3S) at ECMWF. Additionally, to estimate the atmospheric forcing over polynya openings, we computed the open water turbulent heat flux using the Coupled Ocean-Atmosphere Response Experiment (COARE) bulk algorithm version 3.6 (Edson et al., 2013; Fairall et al., 2003), forced with ERA5 atmospheric variables. The sea surface temperature (SST) needed in the calculation was also taken from ERA5, but set to the freezing point of sea water whenever colder (as happens over sea-ice).

Table 1
Composition of Moorings M1 and M2 Deployed on 14 July 2016 Over a 99 m Depth

Depth (m)	Instrument	Variables	Record (days)	Sampling rate (s)
Mooring M1				
14.3	**SBE37**	P, T, S	440.6	1,200
14.3	RBR	T	440.6	4
19.4	RBR	T	440.6	4
24.5	RBR	T	440.6	30
29.5	**SBE37**	P, T, S	440.6	1,200
29.5	RBR	T	440.6	4
34.6	RBR	T	440.6	4
39.6	RBR	T	440.6	30
44.7	**SBE37**	P, T, S	440.6	1,200
44.7	RBR	T	440.6	4
49.7	RBR	T	440.6	4
54.8	RBR	T	311.6	30
59.9	**SBE37**	P, T, S	440.6	1,200
59.9	RBR	T	440.6	4
65.2	RBR	T	440.6	4
70.6	RBR	P,T	440.6	4
74.6	**SBE37**	P, T, S	440.6	1,200
74.6	RBR	T	138.0	30
79.9	RBR	T	440.6	4
85.2	RBR	T	440.6	4
86.9	*ADCP*	P, U,V,W	440.6	6,000
89.4	*Aquadopp*	P,U,V,W	440.6	1,200
90.4	**SBE37**	P, T, S	440.6	1,200
90.4	RBR	T	440.6	4
Mooring M2				
66.7	RBR	T	440.7	4
72.1	**SBE63 + SBE37**	P, T, S, O_2	440.7	3,600
85.8	RBR	P, T	352.5	4

Note. M1 and M2 were deployed a few hundred meters apart at 77°58′N and 20° 12′E. Only instruments recording physical parameters are listed.

The daily SIC at a 6.25 and 3.125 km resolution (Figure 2) were obtained from the Advanced Microwave Scanning Radiometer 2 (AMSR2) instrument on board the GCOM-W1 satellite from the Japanese Space Agency (JAXA). The data, based on the ARTIST sea ice algorithm v5.4 using 89 GHz brightness temperatures (Spreen et al., 2008) were obtained from the Bremen University (https://seaice.uni-bremen.de). AMSR2 data are available since 2012 and SIC data for the period 2002 to 2011 are based instead on AMSR-E (AMSR for EOS) on the NASA satellite Aqua.

In addition we have examined the Barents Sea Sea-Ice Index (BSSII) provided by the EUMETSAT Ocean and Sea Ice Satellite Application Facilities (OSISAF; https://osi-saf.eumetsat.int/products/osi-420), defined as the monthly averaged sea ice extent over the Barents Sea (10–60°E; 72–82°N).

2.3. Polynya Model for Ice Production

The polynya model of Jardon et al. (2014) was adapted to run with AMSR2 SIC observations either at a 6.25 or 3.125 km resolution. Similar to the approach of Haarpaintner, Gascard, and Haugan (2001) and Skogseth et al. (2004), this model distinguishes ice production over open water in the form of frazil ice (V_{fraz}), from continuous ice growth under consolidated ice, including landfast and pack ice (congelation ice production, V_{cong}). However, it is based on a distinct strategy to distinguish open water and ice-covered areas, crudely assimilating daily satellite SIC in a simple ice-thickness classes model instead of relying on a polynya opening model forced by winds. The domain considered by the model (Figure 2), which spans 12,246 km², is restricted to regions north of the 120 m deep sill where BSW accumulates, following Skogseth et al. (2004). This domain is twice as large as the maximal extent of the polynya of 6,000 km² (Haarpaintner, 1999). The volume of the domain is $\mathcal{V} = 850$ km³ (Skogseth, Haugan, & Jakobsson, 2005). Satellite pixels within this domain with more than 5% missing data were discarded so that the final basin spans 9,434 km² (9,842 km²) for the 3.125 km (6.250 km) resolution AMSR2 SIC product. Data gaps were otherwise filled with a linear interpolation in time. The discarded pixels are mostly coastal, occupied by landfast ice or glaciers, with therefore a very limited contribution to the total ice production. The volume of the basin over which ice production is considered is 670 km³ after correction for the cumulative area of discarded pixels (2812 km²) using a depth of 64 m (median over the basin).

The equivalent thickness of frazil ice formed per unit time is proportional to the net air-sea flux over open water Q_{net},

$$\frac{dH_0}{dt} = -\frac{Q_{net}}{\rho_f L_i}, \tag{1}$$

where ρ_f is the density of frazil ice (950 kg m⁻³) and L_i is the latent heat of fusion (234.14×10^3 J kg⁻¹). The turbulent component of Q_{net} is computed using the COARE 3.6 algorithm whereas the radiative part comes from ERA5. The growth rate of congelation ice dH at the bottom of the ice cover is determined from the empirical relation of Maykut (1986) based on Stefan's law, that is, proportional to the cumulative number of freezing-degree days (ζ) computed from ERA5:

$$dH = \frac{12.9}{2H + 16.8} d\zeta, \tag{2}$$

where both dH and H are expressed in cm. The mass of salt (in g) rejected in the ocean when ice forms is computed as by Skogseth et al. (2004):

$$M_{salt} = 0.79 \times S_o \left(\rho_f V_{fraz} + \rho_i V_{cong} \right), \tag{3}$$

where S_o is the initial surface salinity of seawater set to 34.15 for consistency with previous works and $\rho_i = 917$ kg m⁻³. The coefficient 0.79 is the fraction of surface water salinity that is released when ice forms (0.69) augmented by 0.1 to account for additional release when ice ages (Haarpaintner, Gascard, & Haugan, 2001; Martin & Kauffman, 1981).

2.4. Production of BSW: A Model With Linear Stratification

Box models have often been used to estimate the volume of dense water produced in a polynya (e.g., Cavalieri & Martin, 1994). Regarding Storfjorden, a box model approach was used by Schauer (1995), albeit in a reverse mode, to estimate the initial salinity of the source water forming BSW since the volume flux of BSW was directly measured by current meters located at the sill. Building on this approach, Skogseth et al. (2004) estimated the volume of BSW formed, V_{bsw}, assuming that all the salt released during freezing M_{salt} is used to form BSW, which yields an expression based on the difference between the surface salinity of the ocean at the onset of the freezing season S_o and that of the BSW at the end of winter, S_b,
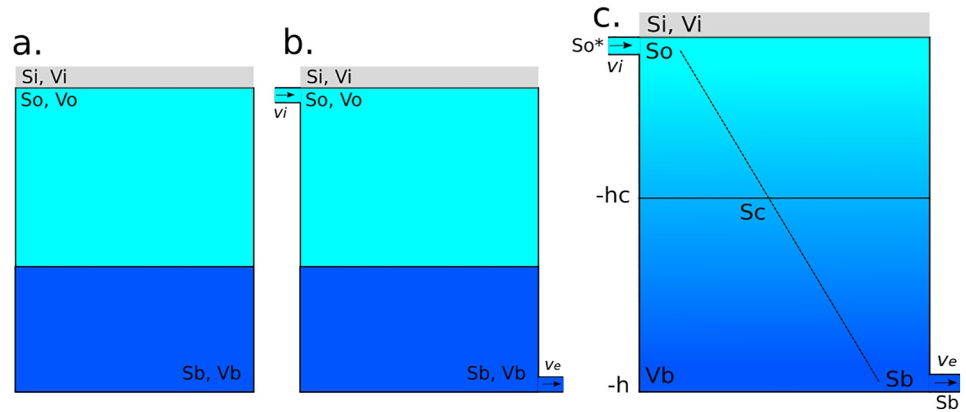
Figure 3. Box models of dense water formation in the polynya. Traditionally the system is composed of three compartments, a sea ice layer of volume V_i, salinity S_i, and density ρ_i topping a two-layer ocean, with the bottom layer representing the dense water being formed with the salt release associated with freezing (panel a). The salinity of each compartment is constant whereas their volume varies. An extension of the model is to include an export of the dense water with volume flux v_e, replaced by surface water with volume flux v_i (panel b). The new model considers a linear vertical stratification in salinity, time-varying, with the reservoir of dense water forming in the polynya defined as waters with a salinity exceeding a critical value $S_c = 34.8$, which is the definition of Brine-enriched Shelf Water (panel c). The exported flux v_e at the bottom has a salinity $S_b(t)$, compensated by an inflow of surface water with constant salinity $S_o^{\star}$.

$$V_{bsw} = \frac{M_{salt}}{\rho_b(S_b - S_o)}. \tag{4}$$

This expression comes from the conservation of mass and salt between three reservoirs: a sea-ice layer of salinity S_i, density ρ_i and volume V_i, topping a two-layer ocean composed of a bottom (BSW) layer with characteristics S_b, ρ_b and volume V_b, surmounted by a layer containing the source water with characteristics S_o, ρ_o and V_o (Figure 3a). Assuming the salinity and density of each layer to be constant, mass and salt conservation equations between time t and $t + \Delta t$ read

$$0 = \rho_o \Delta V_o + \rho_i \Delta V_i + \rho_b \Delta V_b \tag{5}$$

$$0 = \rho_o S_o \Delta V_o + \rho_i S_i \Delta V_i + \rho_b S_b \Delta V_b \tag{6}$$

Substituting ΔV_o into Equation 6 from Equation 5 and further assuming $S_i = \alpha S_o$ with $\alpha = 0.21$ according to Equation 3 yields

$$\Delta V_b = \frac{F_S}{\rho_b(S_b - S_o)}, \tag{7}$$

where

$$F_S = (1 - \alpha)S_o \rho_i \Delta V_i \tag{8}$$

is the mass of salt released into the ocean between t and $t + \Delta t$, the integral form of which was shown in Equation 3.

In the calculations of the salinity of the source water, Schauer (1995) estimated V_{bsw} by measuring the flux leaving the box, which seems to contradict the paradigm of a box model where exchanges are limited to the three compartments defined above. In fact the box model can be amended to allow for an outlet of dense BSW with volume transport v_e, compensated by an inlet in the surface reservoir of water with salinity S_o and volume transport v_i (Figure 3b). Imposing $\rho_b v_e = \rho_o v_i$ for mass conservation, yields

$$\Delta V_b + v_e = \frac{F_S}{\rho_b(S_b - S_o)}. \tag{9}$$

This expression is similar to Equation 7 showing that changes in the BSW volume are partitioned between the local reservoir and an exported part.

In their estimates of V_{bsw}, Skogseth et al. (2004) integrated Equation 7 over the freezing period, taking the value measured in April from a hydrographic profile for S_b, whereas S_o was constructed as a piecewise linear function of time, ranging between the surface salinity measured in the fall prior to the freezing season and that measured in April, and constant afterward. Enabling S_o to increase with time following observations boosts the increase in V_b per unit of salt released by reducing the denominator $S_b - S_o$. While certainly improving the realism of the approach, taking a time varying S_o in Equation 7 relaxes the hypothesis of salt conservation used in the derivation, which is not fully satisfactory. Indeed, enforcing salt conservation while enabling variations in S_o leads to

$$\Delta V_b = \frac{F_S}{\rho_b(S_b - S_o)} - \frac{\rho_o V_o \Delta S_o}{\rho_b(S_b - S_o)}. \tag{10}$$

This expression shows a reduced increase in V_b for a given salt flux since part of this flux is consumed to increase the salinity of the upper layer. Skogseth et al. (2004) are well aware of the underlying approximation and clearly state their assumption that *all released salt during freezing of surface water and corresponding ice aging is used for production of BSW*. This assumption is far from being unrealistic since for most of the winter/spring the water column is entirely filled with BSW, a situation for which the second term of Equation 10 is identically zero $(V_o = 0)$.

Here we go one step further in the set up of a simple model to estimate the volume of BSW produced in the polynya, taking advantage of the fact that salinity profiles are continuously measured over the freezing period. Following Skogseth et al. (2004) we allow the surface salinity $S_o(t)$ to vary in time. In addition, we also enable the bottom salinity $S_b(t)$ to vary in time according to observations. An inflow v_i of surface water with constant salinity $S_o^\star$, set to the initial salinity at the onset of the freezing period compensates for the bottom outflow with volume flux v_e such that $\rho_b v_e = \rho_o^\star v_i$ for mass conservation. Rather than taking a box model with constant salinity layers, we use a linear stratification entirely defined by the surface and bottom values (Figure 3c). The model is detailed in Text S1 and S2 in Supporting Information S1, and only a brief presentation is given below. The BSW reservoir is defined as the layer with salinity exceeding the threshold value $S_c = 34.8$. Its volume is thus

$$V_b(t) = \begin{cases} 0 & \text{if} \quad S_b(t) \leq S_c \\ \mathcal{V}\dfrac{S_b - S_c}{S_b - S_o} & \text{if} \quad S_o(t) \leq S_c \leq S_b(t) \\ \mathcal{V} & \text{if} \quad S_o(t) \geq S_c. \end{cases} \tag{11}$$

The total production of BSW over the freezing season $[t_0, t_f]$ reads

$$V_{bsw}(t_f) = \sum_{t=t_0}^{t_f} v_e(t)\mathcal{H}(v_e) + V_b(t_f), \tag{12}$$

where $\mathcal{H}$ is the Heaviside step function. When $S_b(t) \geq S_c$, the exported BSW volume between t and $t + \Delta t$ can be expressed as

$$v_e(t) = \frac{1}{\rho_b(S_b(t) - S_o^\star)}(F_S(t) - D_S(t)). \tag{13}$$

The bottom outflow is thus proportional to the difference between the flux of salt into the ocean due to freezing, $F_S(t)$, provided by Equation 8, and the salt content variation of the liquid ocean, obtained from the mooring data, approximated to $D_S(t) = \mathcal{V}\rho_o \Delta S_m(t)$, where $S_m(t) = (S_o + S_b)/2$. This simple model is obviously imperfect and
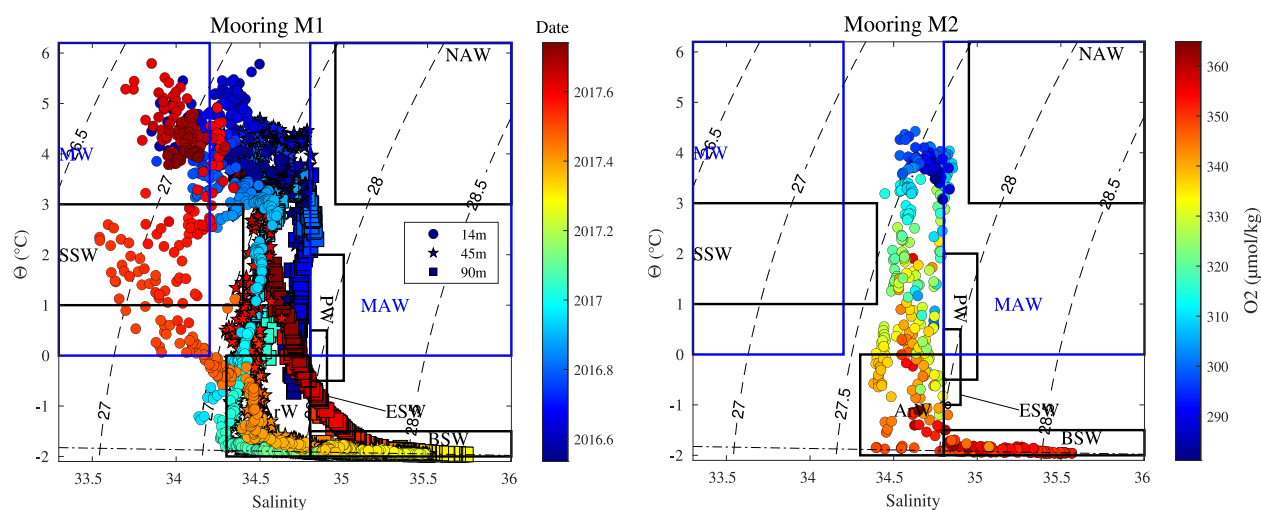
Figure 4. Potential temperature—salinity diagram from SBE-37 at 14, 45, and 90 m at mooring M1 (left) and from SBE-63/SBE-37 at 72 m at mooring M2 (right). The color denotes the time in fractional year (left) and the dissolved O_2 concentration in μmol kg^{-1} (right). See text for the acronym of water masses.

we provide a rough metrics for the error in Text S2 in Supporting Information S1, as well as additional details regarding the tuning procedure.

3. Results

3.1. Evolution of Water Masses

3.1.1. Mooring

The evolution of physical properties of the water masses sampled by SBE-37 sensors is shown in the form of Θ-S diagrams (Figure 4) and Hovmöller diagrams (Figure 5). A stick-plot of horizontal currents at successive depths is superimposed in Figure 5 (top).

Schematically, two main water masses, separated by the PF, occupy the northwestern Barents Sea (Loeng, 1991): cold and fresh Arctic Water (ArW; $\theta \le 0.0$°C and $34.3 \le S \le 34.8$) on the northern side and warm and salty North Atlantic Water (NAW; $\theta > 3.0$°C and $S > 35$) on the southern side. Other water masses are locally formed, either from a transformation of one of the above due to buoyancy forcing at the air-sea interface or from mixing.

Here, five different water masses are identified in the record; these are labeled following the classification compiled by Skogseth, Haugan, and Jakobsson (2005). Starting in Summer 2016, the upper 30 m of the ocean were only sporadically occupied by Melt Water (MW; $\theta > 0.0$°C and $S < 34.2$) until late October.

While pure NAW was not found as far north, we identify two subsurface intrusions of Modified AW (MAW; $\theta > 0.0$°C and $S > 34.8$) below 50 m in August 2016 and closer to the bottom in October 2016. This water mass, which results from the mixing of NAW and ArW along the PF, is traditionally observed in Storfjordrenna, south of the 120 m sill (Schauer, 1995; Skogseth, Haugan, & Jakobsson, 2005). Such a northward intrusion of water of Atlantic origin is unusual and was documented for the first time from the CTD stations of the July 2016 cruise (Vivier et al., 2023). This admixture of AW was present at depth for most of Fall 2016. While there were occasional, slightly saltier pulses having clearly the characteristics of MAW, the water mass below 50 m was generally on the definition edge, slightly fresher than the lower bound of 34.8. These saltier pulses were associated with a northward velocity (Figure 5, top), and ended with a reversal of the direction of the current, consistent with a northward spreading of MAW along the east flank of Storfjorden.

Storfjorden Surface Water (SSW; $1 \le \theta \le 3.0$°C and $S < 34.4$), a product of the mixing of ArW and MW subsequently heated by the solar radiation, is generally found in the upper 60 m in summer (Haarpaintner,
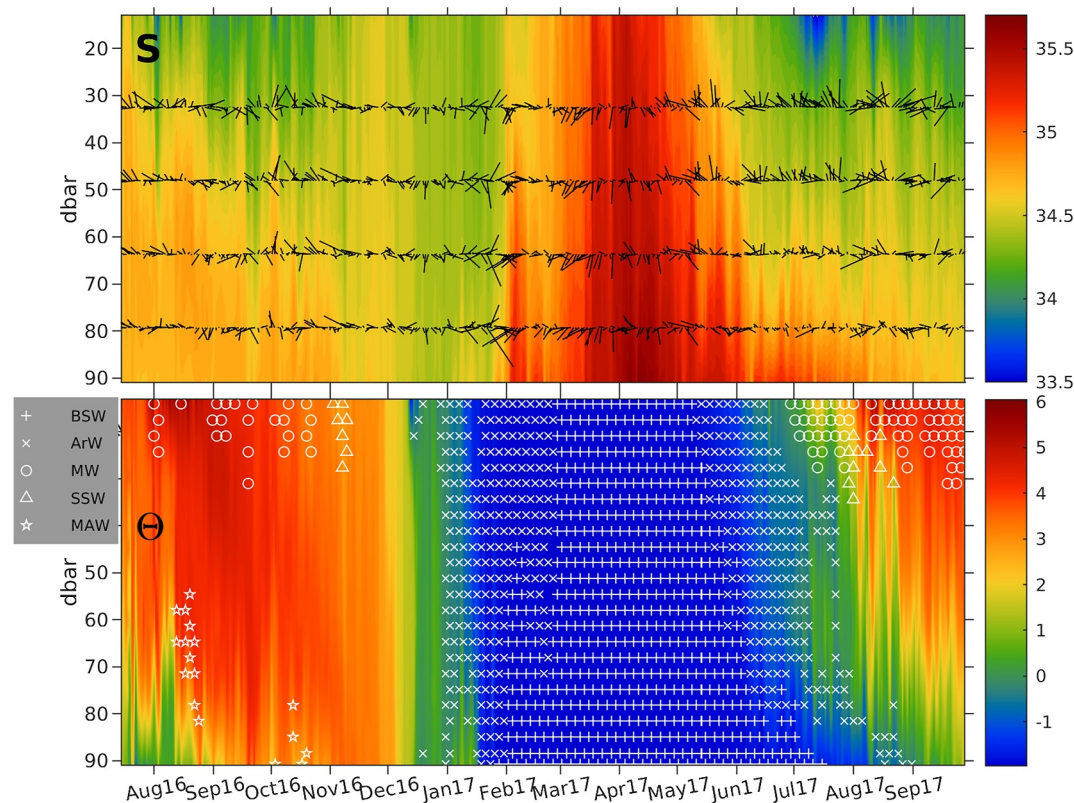
Figure 5. Hovmöller diagrams of salinity (top) and potential temperature (bottom) from mooring M1 SBE-37 sensors between 14 July 2016 and 28 September 2017 (temperature units in ℃). The horizontal velocity at four depths is superimposed as a stick-plot diagram in the top panel. Main water masses are identified by symbols in the bottom panel (see text for the acronym of water masses).

O'Dwyer, et al., 2001). In Summer-Fall 2016, SSW was only briefly found early November in the upper 30 m. This remarkable near absence of SSW, replaced by a saltier water, that was first noted during the July 2016 deployment cruise, thus persisted through the fall.

As of mid-December 2016, ArW occupied the entire water column. The locally formed BSW ($\theta < -1.5℃$ and $S > 34.8$) first appeared at the bottom late January 2017, before filling the entire water column as of March 2017, until mid-May 2017. BSW was subsequently replaced by a layer of ArW extending progressively from the surface to greater depth. BSW was found at the bottom until mid-July 2017, in great contrast with the water mass distribution of July 2016. The maximum BSW salinity, recorded on 10 April 2017 at 90 m, was 35.74 (35.77) for 4-hr low pass filtered (instantaneous) data corresponding to a potential density anomaly of $\sigma_\theta = 28.79$ kg m^{-3} ($\sigma_\theta = 28.82$ kg m^{-3}). Although subsequent dilution with ambient water likely occurs on the descent to the main depression of Storfjorden, the BSW formed in Winter 2016–2017 is definitely on the saline and dense side. The formation of BSW was associated with a drastic change in the currents, which strengthened and took on at all depths a relatively steady orientation toward the south-southwest (Figure 5, top), that is in the direction of the main depression of Storfjorden. This indicates a gravity drainage of the saline water from the shallow areas into the deeper part of the fjord. This drainage is particularly clear in progressive vector diagrams (the curves obtained by accumulating the velocity vectors with time) in which we see the predominantly northward trajectories at all depths sharply switching to the southwest with the increase of potential density, before gradually resuming a northward trajectory from the surface to depth with the restratification of the water column (Figure 6). Also noteworthy in Figure 6 is the substantial cyclonic veering with depth observed at the deepest record, 10 m above the bottom. The latter is consistent with that expected from an Ekman spiral induced by bottom friction. A reasonable fit to an Ekman spiral is obtained for the period when BSW is present,
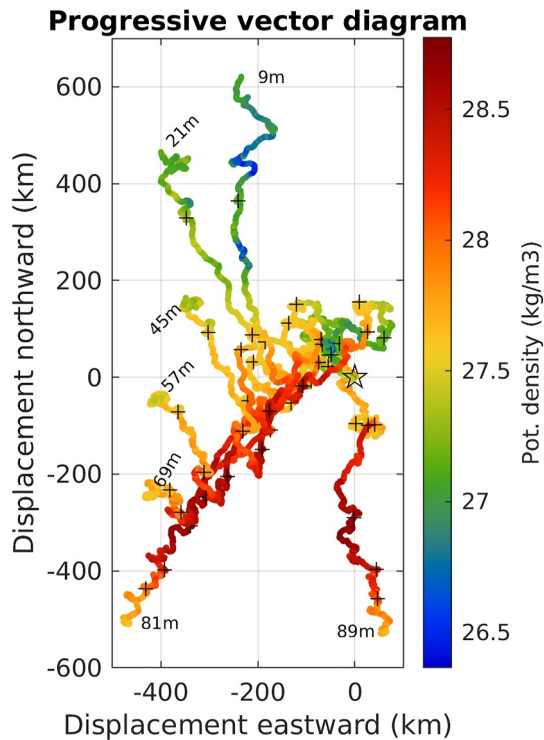
Figure 6. Progressive vector diagrams of the currents recorded at mooring M1 at different depths between July 2016 and September 2017. The color denotes the potential density at the corresponding depths (units in kg m^{-3}). The black star denotes the origin whereas black crosses along trajectories are bimonthly tick marks.
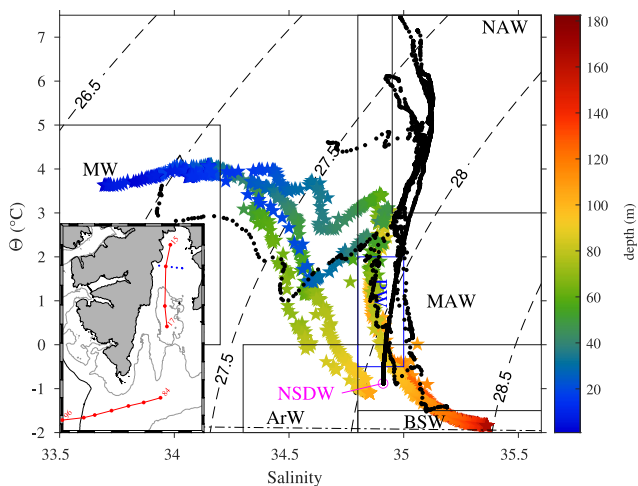

Figure 7. Potential temperature—salinity diagram of four conductivity-temperature-depth (CTD) stations forming the meridional section in Storfjorden (colored stars) and seven CTD stations forming the meridional section in Storfjordrenna (black dots) occupied in Summer-Fall 2017. The meridional section of Storfjorden, intersecting the main depression, was occupied during the STEP 2017 recovery cruise (28–29 September 2017); The zonal section in Storfjordrenna from the IOPAN AREX cruise was occupied on 1 July 2017. The 120 m (gray line) and 500 m isobaths (black line) are shown in the inset map. See text for the acronym of water masses.

assuming a constant viscosity of $\nu = 5 \times 10^{-3}$ m^2 s^{-1}, yielding a bottom layer thickness of 8.4 m (Text S3 in Supporting Information S1).

Summer-Fall 2017 contrasted with its 2016 counterpart, with a much larger presence of MW in the upper 30 m (Figure 5). Likewise, SSW was found in August 2017 down to 40 m but remained much less abundant than what could be expected from historical observations (Haarpaintner, O'Dwyer, et al., 2001). Instead, the water in the upper 60 m was warmer and saltier than the SSW with its known characteristics before 2005. At the bottom, Figure 4 (left) indicates that the water had the characteristics of East Spitsbergen Water (ESW; $-1 \leq \theta \leq 0.5°$C and $34.8 \leq S \leq 34.9$). ESW, like MAW and PF Water (PW), is formed through mixing between NAW and ArW along the PF. It was originally identified to form west of Hopenbanken and brought about by the East Spitsbergen Current (Quadfasel et al., 1988). Here the water seems to have formed from the mixing of BSW, which is different from the previous mechanism: its classification as ESW does not therefore seem appropriate.

The dissolved O_2 concentration at 70 m ranged between a minimum of 280 μmol kg^{-1} for the MAW sampled in October 2016 to a maximum of 365 μmol kg^{-1} for ArW in June 2017 (Figure 4, right). It presents a pronounced seasonal cycle, gradually increasing from mid-October to January as surface cooling promotes convection and associated diapycnal mixing of the colder thus more oxygenated surface water. It nearly plateaued at 350 μmol kg^{-1} between February and June as the entire water column was ventilated (BSW formation), before starting to decrease until the fall, following the restratification of the water column.

3.1.2. Storfjorden Hydrography in September 2017

As BSW is being formed in winter-spring throughout Storfjorden, it flows toward the main depression of Storfjorden where it accumulates before spilling over the sill into Storfjordrenna during spring-summer (e.g., Skogseth, Haugan, & Jakobsson, 2005). Although the allotted ship time for the September 2017 recovery cruise did not permit a comprehensive sampling of Storfjorden, nine CTD stations (14–22) were nevertheless occupied (Figure 1). These profiles made it possible in particular to measure the properties of remnant BSW at the deepest points in Storfjorden. The Θ-S diagram of the stations along a meridional section intersecting the main depression is shown in Figure 7. The densest BSW ($\sigma_\theta = 28.47$ kg m^{-3}) was found at the bottom of Station 17 in the southern part of the main depression with a salinity of 35.36. There, BSW was found at depth greater than 115 m (Figures 8a and 8b), that is slightly above the sill depth, suggesting that the BSW reservoir had not completely flushed out yet, and that an overflow might still have been present at the sill located 20 km to the south. Remnant BSW was also sampled at the bottom of Station 16 still in the main depression at depths larger than 140 m (Figure 8). Although water colder than the −1.5°C threshold for BSW was only found below 115 m, the main depression was occupied by particularly dense and saline water. At Station 17 the 34.8 isohaline was located at 40 m depth and the $\sigma_\theta = 28.00$ kg m^{-3} was at 80 m depth, well above the sill level. The BSW layer was overlain by a layer of PW and MAW, between 40 and 110 m, indicating an intrusion of water of Atlantic origin up to 77° 45' N. Water of Atlantic origin thus penetrated into Storfjorden for the second summer in a row although this September 2017 intrusion was not as massive and as far reaching as the MAW intrusion reported in
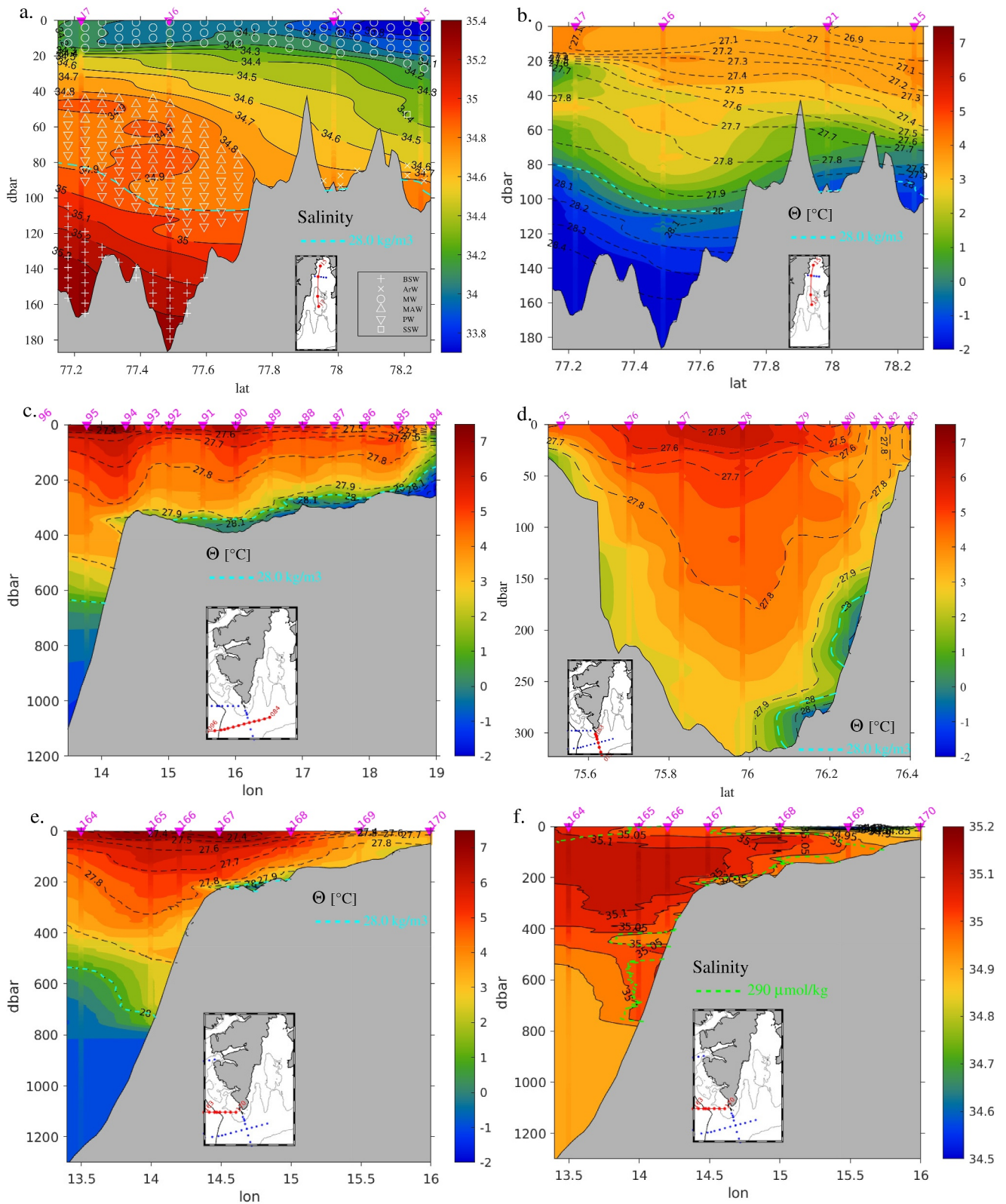
Figure 8.

July 2016 (Vivier et al., 2023). In the northern part of Storfjorden, the bottom was occupied by a mixture of PW and BSW, overlain by a thin (~10 m) layer of remnant ArW. Contrary to the July 2016 cruise, MW was ubiquitously found in the upper 20 m. SSW, however, remained nearly absent, replaced by a water mass saltier than the 34.4 threshold.

3.1.3. Spreading of the BSW Overflow in Storfjordrenna

Three CTD sections from the July 2017 IOPAN AREX survey, covering Storfjordrenna and the shelf break west of Sørkapp, made it possible to document the dense plume associated with the BSW overflow. A subset of the stations of the zonal section along Storfjordrenna is shown in the θ-S diagram in Figure 7. The westernmost station considered here (Station 96) located on the shelf break over a depth of 1,400 m displays a θ-S relationship typical of the Norwegian/Greenland Sea with a layer of Norwegian Sea Deep Water (NSDW), identified by a salinity of 34.91 and a potential temperature around $-1°C$ (Langehaug & Falck, 2012; Schlichtholz & Houssais, 1999; Swift et al., 1983), overlain by the AW layer limited at its base by the $\sigma_\theta = 27.97$ kg m^{-3} isopycnal (Rudels et al., 2005). At the easternmost station (Station 84), the θ-S relationship was radically different, resembling that found in Storfjorden with BSW at the bottom, MW at the surface and MAW at intermediate depths. Consistently with the particularly dense and saline BSW sampled in Storfjorden, the plume was well characterized in Storfjordrenna at Station 84, ~ 90 km downstream of the sill, with bottom potential temperature of $\sim -1.5°C$, a salinity of 35.19 and a maximum density of $\sigma_\theta = 28.32$ kg m^{-3} (Figure 7).

Further downstream in Storfjordrenna, the density of the bottom plume diminished with the entrainment of ambient water but remained denser than 28.10 kg m^{-3} up to Station 90, at 16°W, west of Sørkapp's longitude (Figures 7 and 8c). The plume does not have the two-layer vertical structure observed by Fer et al. (2003), with a denser layer attributed to the remnants from the previous overflow; it instead shows up as a homogeneous layer (50 m thick at Station 90) consistent with the fact that the plume was much lighter in 2016 than in 2017. Although remaining particularly dense, the bottom layer water was not cold enough to be defined as BSW west of Station 84. The bottom plume shoulders the northern flank of Storfjordrenna as is visible at the meridional section at Sørkapp (Figure 8d), consistent with previous modeling and observational studies (Akimova et al., 2011; Fer & Ådlandsvik, 2008; Fer et al., 2003). These studies further showed that its path bends northward along the western continental slope of Spitsbergen. The plume modeling works of Wobus et al. (2013), including tides, revealed that the plume forks into two branches after the Sørkapp headland: a deep branch that sinks down the slope while the lighter water from the plume is diverted onto the shallow shelf as part of the Spitsbergen Polar Current/Sørkapp Current. West of Station 90 the bottom topography rises by 50 m up to Station 94 owing to the presence of a submarine mound (likely the remnants of a terminal moraine) overhanging the shelf break (Figure 1). The cold plume remains visible at Station 94 over the shelf break at 340 m depth with a substantially smaller density anomaly of $\sigma_\theta = 27.96$ kg m^{-3} (Figure 8c), suggesting that the densest plume has cascaded north of this mound.

With a core density in excess of 28.10 kg m^{-3}, if not too diluted by slope convection down the West Spitsbergen Shelf break, the dense plume in Storfjordrenna could insert underneath the AW layer ($\sigma_\theta \leq 27.97$ kg m^{-3}; Rudels et al., 2005) and feed the deep water layer. The zonal hydrographic section on the shelf break west of Sørkapp (Stations 163–170) tends to confirm this scenario (Figures 8e and 8f). At first sight, the plume is identified as a cold bottom anomaly at Stations 167–168 on the shelf at 200 m depth (Figure 8e). This is actually the shallow branch modeled by Wobus et al. (2013), whereas there is evidence of two deep branches on the shelf slope at Stations 165–166 at 400–450 m depth and 500–750 m. They appear as a warm anomaly (1.7–2.4°C; Figure 8e) due to the entrainment of warm AW (Akimova et al., 2011; Quadfasel et al., 1988). The deepest branch has a salinity in excess of 35.00 (Figure 8f) well above the salinity of NSDW (34.91) and its density at the bottom reaches 28.00 kg m^{-3}. Finally, the different branches of the plume, both on the shelf and the shelf slope, are

Figure 8. Hydrographic sections in Storfjorden (top), Storfjordrenna (middle) and on the shelf break west of Sørkapp (bottom) in Summer-Fall 2017. The top plots show a meridional section of salinity (a) and potential temperature with isopycnals superimposed (b) along Storfjorden occupied on 28–29 September 2017 during the STEP-2017 cruise. Water masses are identified in (a). The middle panels display the potential temperature (color scale) with potential density contours superimposed in a zonal section along Storfjordrenna (c) and a meridional section south of Sørkapp (d) occupied on 1 July 2017 (AREX survey from IOPAN). The bottom plots show the potential temperature (color scale) with potential density contours superimposed in a zonal section occupied on 15 July 2017 west of Sørkapp (e) and the salinity on the same section with the 290 μmol kg^{-1} dissolved oxygen concentration isopleth superimposed (f). In panels (a)–(e), the $\sigma_\theta = 28.00$ kg m^{-3} isopycnal is highlighted to mark the Brine-enriched Shelf Water overflow.

clearly identified by their high dissolved O_2 concentration in excess of 290 μmol kg^{-1} (Figure 8f). BSW is indeed a highly oxygenated water mass with a concentration of 350 μmol kg^{-1} measured in Storfjorden (Figure 4, right) and concentrations $\geq$300 μmol kg^{-1} measured in the bottom plume in Storfjordrenna (not shown).

3.2. Atmospheric Forcing and Sea-Ice Cover in 2016–2017

Additional data were analyzed to gain insight into the evolution of water masses in Storfjorden depicted above (e.g., Figure 5). We have first examined the satellite SIC data over Storfjorden. Winter 2016–2017 was marked with a particularly delayed and shortened ice season. Sea ice first appeared on 16 January 2017, 57 days later than the average, and remained until 16 June 2017, 8 days in advance compared to the average date for an ice-free fjord (not shown). Indeed, on average over the 2002–2019 period, sea ice started forming in Storfjorden as of year-day 324 (20 November) whereas the fjord was free of ice as of year-day 175 (23 June). The 2016–2017 ice season lasted therefore only 152 days instead of the average 216 days.

Winds and air temperature from ERA5 are displayed in Figure 9 jointly with their monthly average and standard deviation computed from 11 years of hourly data (2010–2020). The top plot is the Ekman transport into Storfjorden F_{Ek} defined, following Geyer et al. (2009), as the zonal integral of the zonal wind stress τ_x along 76.5° N, $F_{Ek} = -\int_{18°E}^{21°E} \tau_x / (\rho_0 f) \, dx$, where f is the Coriolis parameter and ρ_0 the density of sea water. For the purpose of the present discussion it can be viewed as the negative of the average zonal wind stress in the region. Fall 2016 appears strongly anomalous with air temperature well above average, and consistently one standard deviation above average until late November (Figure 9c). Likewise, October was characterized with strong westerlies rather than northeasterlies typical for October conditions (Figure 9a). Except for brief episodes in October, negative air temperatures were not experienced until late November, followed by a strong warming in December associated with southwesterlies. These anomalous atmospheric conditions explain the late freezing of Storfjorden. The ocean was indeed anomalously warm in the fall. Mohamed et al. (2022) analyzed the occurrence of marine heat waves from SST data and found a 69 days heat wave in the northern Barents Sea, from 29 September to 6 December 2016, with a mean (maximum) intensity of 1.55°C (2.15°C). Negative air temperatures really picked up in January, which corresponds to the onset of freezing as detected in SIC data. A strong rise in temperature associated with southwesterlies was experienced during the first half of February, before reversing to cold air temperatures brought about by strong northeasterlies. March, when BSW starts occupying the entire water column (Figure 5b) was substantially colder than average. Air temperature subsequently gradually increased during Spring 2017, with May notably colder than average (Figure 9c). Spring 2017 was also characterized by five outstanding northeasterlies episodes, which are conditions prone for polynya openings. Positive air temperatures were finally reached early June, shortly before the disappearance of sea ice in Storfjorden.

3.3. Ice Production in the Polynya

The polynya model described in Section 2.3 was run between 16 January and 16 June 2017, when ice was present in the fjord according to satellite observations (ice season). The freezing season was shorter, however, with net air-sea fluxes switching durably to positive values (ocean warming) as of 14 May 2017 (not shown). It thus lasted 119 days.

The reference simulation was based on the 3.125 km resolution SIC satellite data and assumed an initial ice thickness of 5 cm, further imposing the export of ice classes thicker than 120 cm (see Jardon et al., 2014). The total volume of ice formed was 44.2 km^3, mostly contributed by frazil ice with a volume V_{fraz} of 37.1 km^3 (Figure 10). The increase of V_{fraz} occurs by steps, corresponding to polynya opening episodes. An example of such an episode in late March 2017 is displayed in Figure 2. It was triggered by strong northeasterlies and associated with air temperatures below -17°C (Figure 9). The strong heat loss from the ocean (400–600 W m^{-2}, not shown) generated $\sim$4 km^3 of frazil ice in one week (Figure 10).

An ensemble of simulations was performed using different initial ice thicknesses, model settings (disabling import/export of sea ice from the fjord, enabling a parameterization of surface melt), and both 3.125 and 6.250 km resolution satellite SIC products. The simulated volume of frazil ice remained relatively robust, ranging from 37.1 to 38.2 km^3. V_{fraz} is primarily sensitive to the open water area provided by AMSR2 satellite data, but otherwise relatively independent of the different model options. Here the use of the coarser 6.250 km resolution SIC data gave a slightly larger V_{fraz}. The total volume of ice formed ranged between 40.2 and 45.5 km^3, with the
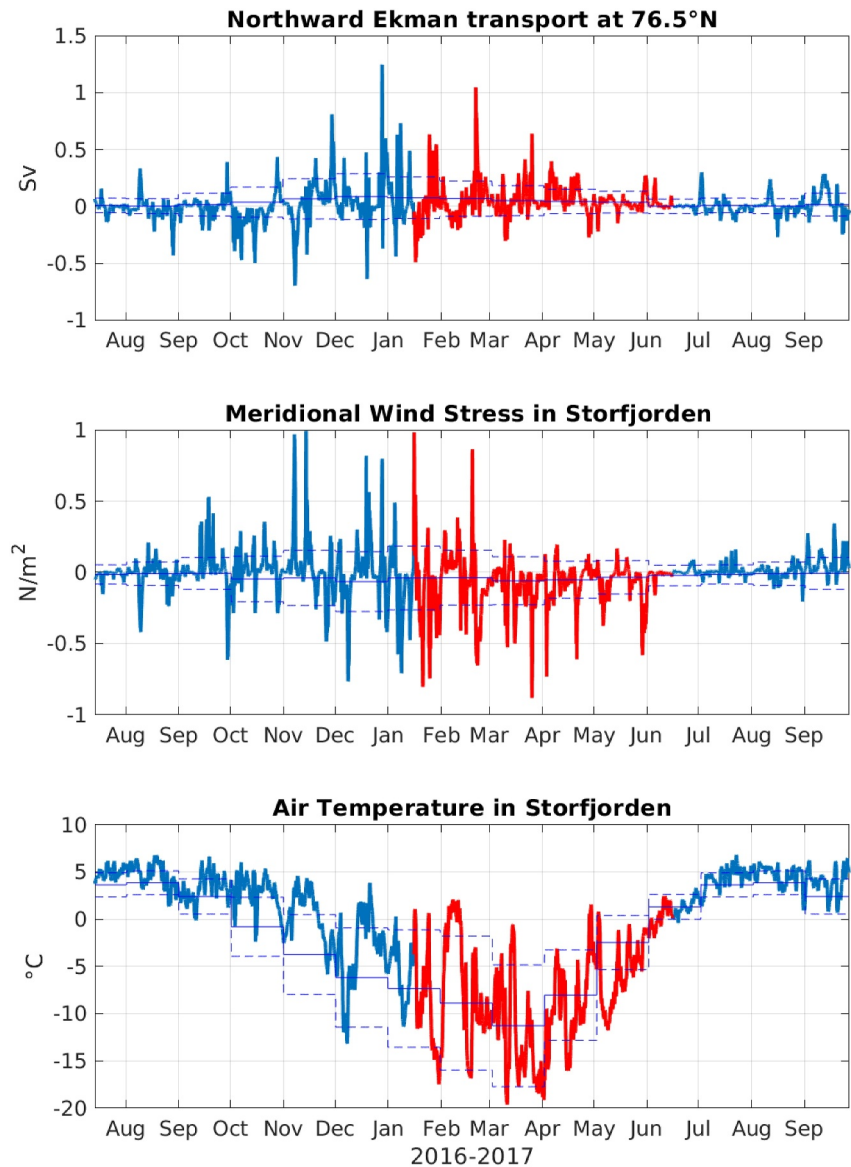
Figure 9. Time series of Ekman transport into Storfjorden at 76.5°N integrated between 18°E and 21°E (top), Meridional wind stress (middle) and 2 m air temperature (bottom) averaged over Storfjorden. The 2010–2020 monthly average and standard deviation from the monthly average are denoted by the solid and the dashed thin blue lines, respectively. The red segment denotes the period during which sea ice was present in Storfjorden. In the top plot, a positive Ekman transport corresponds to a negative (westward) zonal wind stress.

congelation ice production V_{cong} being more sensitive to the parameterizations influencing the ice-thickness distribution. Indeed, the growth rate of congelation ice at the bottom of the ice cover is inversely proportional to ice thickness according to the empirical relation of Maykut (1986) (Equation 2). The total mass of salt released according to Equation 3 was $1,126 \times 10^9$ kg for the reference run, ranging between 1,028 and $1,160 \times 10^9$ kg for the ensemble of simulations.

3.4. Production of BSW

The volume of BSW formed in Storfjorden, V_{bsw}, was estimated from the salt flux stemming from the ice production model and salinity observations provided by the mooring.
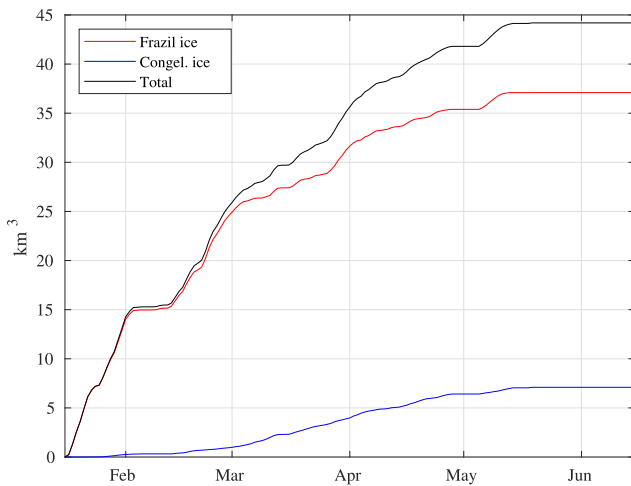
Figure 10. Accumulated volume of frazil and congelation ice between 16 January and 17 June 2017 according to the polynya model. Units in km^3.

3.4.1. Regular Box Model

We first used the regular slab-layer version of the box model defined by Equation 4. The surface salinity of the ocean at the onset of the freezing season S_o was 34.28, taken from the shallowest SBE37 at 15 m depth on 16 January 2017. At the end of the freezing season, on 14 May 2017, S_{bsw} was 35.38 at 90 m depth (Figure 11; top). This value is consistent with the salinity of 35.36 of the residual BSW measured at the bottom of the main depression of Storfjorden in July 2017. Integration of Equation 4 yields $V_{bsw} = 995$ km^3, which exceeds the entire volume of the Storfjorden basin. This value of V_{bsw} corresponds to a mean volume transport of 0.097 Sv over the 119 days of the freezing season, or 0.032 Sv when annually averaged (Table 2).

For the sake of comparison, we also estimated V_{bsw} following the approach of Skogseth et al. (2004), that is based on the time integration of Equation 4 using a piecewise linear profile for $S_o(t)$ while S_{bsw} is held constant at the end of winter value. As previously S_{bsw} was set at 35.38, which is the value recorded at 90 m depth on 14 May 2017 (end of the freezing season). Based on the record of the SBE37 at 15 m, S_o was linearly increased from 34.28 (16 January 2017) to 34.69 (14 May 2017) and held constant afterward. This

approach increases V_{bsw} to 1,207 km^3, corresponding to a mean volume transport of 0.117 Sv over the freezing season or 0.038 Sv for the annual average (Table 2).

In their study, Skogseth et al. (2004) used available CTD profiles to determine the salinity at the onset of freezing and at the end of the freezing period. For the latter they used observations from cruises that all occurred mid-April,
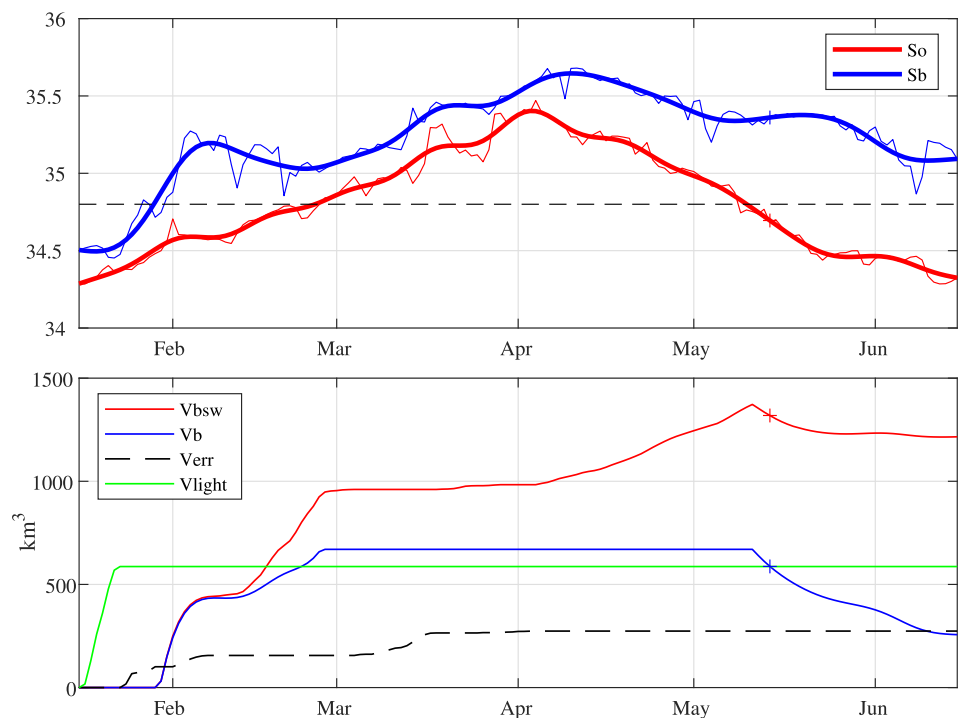

Figure 11. (top) Daily averaged value of near-surface salinity S_o and near-bottom salinity S_b from the mooring, together with their 14 day low-pass filtered counterpart used to run the Brine-enriched Shelf Water (BSW) production model between 16 January and 17 June 2017. (bottom) Volume of BSW produced in the polynya $V_{bsw}(t)$ since 16 January 2017 according to Equation 12 of the box model with linear stratification (red line), which includes the accumulated exported flux and the volume of BSW remaining in the domain $V_b(t)$ according to Equation 11 (blue line). V_{light} is the volume of dense water fresher than 34.8 (green line), thus not identified as BSW. An estimate of the cumulative error V_{err} is also displayed (black dashed line). Units in km^3.

Table 2
Production of Brine-Enriched Shelf Water (BSW) V_{bsw} and Corresponding Transport T_{bsw} Reported to the Duration of the Freezing Period (119 Days in 2017) and Annually Averaged

Year	Method	Ice volume (km^3)	S_o	S_b	V_{bsw}(km^3)	T_{bsw}(Sv)	T_{bsw} (annual mean; Sv)
2017	Equation 4	44.2	34.28[a]	35.38[b]	995	0.097 (119d)	0.032
2017	Equation 4[c]	44.2	34.28[a]–34.69[b]	35.38[b]	1207	0.117 (119d)	0.038
2017	Equation 4	44.2	34.28[a]	35.65[d]	799	0.078 (119d)	0.025
2017	Equation 4[c]	44.2	34.28[a]–35.28[d]	35.65[d]	1541	0.150 (119d)	0.049
2017	**Equation 12**	**44.2**	$S_o(t)$	$S_b(t)$	**1318**	**0.129 (119d)**	**0.042**
1992[e]	Outflow	57[f] (80)		35.1	1600	0.13 (150d)	0.05
1998[g]	Equation 4[c]	38.9	33.90–34.30	35.05	1050	0.067 (182d)	0.033
1999[g]	Equation 4[c]	35.9	33.40–33.60	35.18	860	0.060 (166d)	0.027
2000[g]	Equation 4[c]	44.8	34.09–34.67	35.45	1110	0.068 (188d)	0.035
2001[g]	Equation 4[c]	38.7	34.14–34.42	35.25	1050	0.065 (188d)	0.033
2002[h]	Equation 4[c]	60.0	34.03–34.81	35.83	1090	0.06 (201d)	0.04
2004-2006[i]	Outflow					0.05 (180d)	0.028

Note. The year refers to the end of the freezing season. For 2017 (this study) S_o is taken from the SBE37 recorder at 15 m and S_b from the recorder at 90 m (low pass filtered values with a 14 day cut-off period). For S_o, a range of values indicates a piecewise linear $S_o(t)$. [a]On 16 January 2017. [b]On 14 May 2017. [c]Based on Equation 4 with piecewise linear $S_o(t)$. [d]On 14 April 2017. [e]Reproduced from Schauer (1995); moorings 30 km south of the sill. [f]80 km^3 rescaled to 57 km^3 by Skogseth, Fer, and Haugan (2005) for regions north of the sill. [g]Reproduced from Skogseth et al. (2004). [h]Reproduced from Skogseth, Fer, and Haugan (2005). [i]Reproduced from Geyer et al. (2009); moored ADCP at the sill.

at least 1 month before the end of the freezing period. For a direct comparison with their approach, we also provide estimates of V_{bsw} taking the salinity on 14 April, when BSW is densest, both for S_b and for the spring value at the surface S_o. The near-surface salinity on 14 April 2017 was 35.28: the entire water column at the mooring location was thus filled with BSW, which was not the case for any of the 4 years analyzed by Skogseth et al. (2004), with profiles taken further south over the deep pool of Storfjorden. Using the mid-April 2017 salinity values, the volume of BSW increases to 1,541 km^3 for the box model with piecewise linear surface salinity as per Skogseth et al. (2004), while it reduces to 799 km^3 for the regular box model owing to the larger S_b (Table 2).

3.4.2. Linearly Stratified Box Model

The box model with linear stratification described in Section 2.4 was run to estimate V_{bsw}. We used a basin volume $\mathcal{V} = 670$ km^3 which corresponds to the region actually considered in the ice production model (Section 2.3), and input variables S_o and S_b were low-pass filtered with a cut-off period of 14 days (Figure 11, top), determined from the tuning procedure (Text S1 in Supporting Information S1).

The evolution of V_{bsw} as defined by Equation 12 is shown in Figure 11 (bottom). Also shown in the Figure is the volume of BSW remaining in the domain V_b defined by Equation 11. During the first few days of the simulation, the release of salt from sea ice generates the formation of a volume of ∼600 km^3 of dense water (V_{light}), but this water is not dense enough to be classified as BSW. It is only as of late January that the bottom salinity S_b exceeds the 34.8 threshold value (Figure 11, top) and that the formation of BSW proper starts. Initially, the salt flux F_S from the ice production model matches well with changes in the salt content D_S so that V_{bsw} closely follows V_b until mid February. After that date, F_S exceeds D_S yielding an exported flux ve so that V_{bsw} is subsequently decoupled from V_b. The basin is entirely filled with BSW by the end of February, when S_o exceeds the threshold of 34.8 (Figure 11, top). Accordingly V_b plateaus to a value of 670 km^3 until early May, close to the end of the freezing season (Figure 11, bottom), after which it starts decreasing following the decrease of S_o below 34.8. On the other hand, V_{bsw} keeps on increasing with continuous salt release during the freezing season. It slightly decreases near the end of the freezing season owing to model errors, while one would intuitively expect it to remain constant. This issue is discussed in Text S2 in Supporting Information S1. The evolution of the cumulative model error (V_{err}) is indicated in Figure 11: as stated in Text S1 in Supporting Information S1, it maxes at a value of 270 km^3. The value of V_{bsw} found at the end of the freezing period is 1,318 km^3, larger than previous estimates

Table 3
Ice Production in the Storfjorden Polynya (Mean ± SD)

Period	Method	Ice volume (km³)	Salt release (×10⁹ kg)	Reference
1992	Polynya model	57[a] (80)		Schauer (1995)
1998–1999	Polynya model	28.5 ± 3.3		Haarpaintner, Haugan, and Gascard (2001)
1998–2001	Polynya model	39.6 ± 3.7	995 ± 100	Skogseth et al. (2004)
1998–2002	Polynya model	43.7 ± 9.7	1099 ± 248	Skogseth, Fer, and Haugan (2005)
1970–2002	Polynya model[b]	39.9 ± 11.7		Skogseth, Fer, and Haugan (2005)
2004	Polynya model	48.4		Skogseth et al. (2008)
2006	Polynya model	24.9		Skogseth et al. (2008)
2003–2011	Polynya model	46.9 ± 7.9	1196 ± 200	Jardon et al. (2014)
1992–2007	SSM/I	137 ± 35		Tamura and Ohshima (2011)
2003–2011	AMSR-E	47 ± 5		Iwamoto et al. (2014)
1999–2009	NEMO + LIM3.6	33		Rousset et al. (2015)
2002–2014	MODIS	28.3 ± 8.5[c]		Preußer et al. (2015)
2017	**Polynya Model**	**44.2**	**1,126**	**This study**

Note. The year corresponds to the end of the freezing season: for example, 1992 refers to the ice production during Winter 1991–1992. [a]80 km³ rescaled to 57 km³ by Skogseth, Fer, and Haugan (2005) for regions north of the sill. [b]In a degraded mode (no tuning of the model with ERS2 data before 1997). [c]Estimate for the period November–March only.

with the regular box model except for that based on a piecewise linear salinity profile with mid-April values as per Skogseth et al. (2004). This corresponds to a mean transport of 0.129 Sv during the 119 days of the freezing period or 0.042 Sv for the annual average (Table 2). We further note the overall consistency of the results of the more sophisticated box model developed here and that based on the approach of Skogseth et al. (2004), confirming that the approximations underpinning the latter were justified.

4. Discussion

4.1. Sea-Ice Production

In this section, we first aim at appreciating how important the 2016–2017 ice production of 44.2 km³ was relative to available estimates for previous years, which are summarized in Table 3.

Many of these estimates stem from a surface heat balance applied to a wind-driven polynya model tuned with ERS-2 SAR observations, run for different periods (Haarpaintner, Haugan, & Gascard, 2001; Skogseth et al., 2004, 2008; Skogseth, Fer, & Haugan, 2005), with an average production of ∼ 40 km³ per year extending to ∼ 44 km³ when the outstanding year 2002 is included. Schauer (1995) estimated the total sea-ice production of 80 km³ for the winter 1991–1992. However this was for a domain larger than that usually considered by other studies, extending beyond the sill: the 1992 production reduces to 57 km³ after applying the appropriate surface scaling (Skogseth et al., 2004). Another polynya model is that of Jardon et al. (2014), based on a simple ice class model nudged to AMSR-E data, which yielded an average annual production of ∼ 47 km³ for the 2002–2011 period. The same model was used here with AMSR2 data thus methodological biases are probably minimal, making the comparison particularly relevant, although it is important to caveat that the SIC data and atmospheric forcing products are not homogeneous between the two studies. Sea-ice production was also estimated from different remote sensing techniques. Thin ice thickness can be retrieved from microwave imagery, a frequency band unaffected by clouds and for which the brightness temperature is sensitive to the surface salinity: the latter is inversely related to the ice thickness as brine drains out with ice growth (e.g., Martin et al., 2004; Tamura & Ohshima, 2011). Using SSM/I observations between 1992 and 2007, Tamura and Ohshima (2011) found an average production of 137 ± 35 km³ (±SD) for the Storfjorden polynya. This large value was revised by Iwamoto et al. (2014) to an average of 47 ± 5 km³ for the period 2003–2011 using higher resolution AMSR-E observations and an improved algorithm. Their estimate is remarkably consistent with that of Jardon et al. (2014) for the same period (although the methods are different, both estimates rely on AMSR-E data). Other estimates are based on
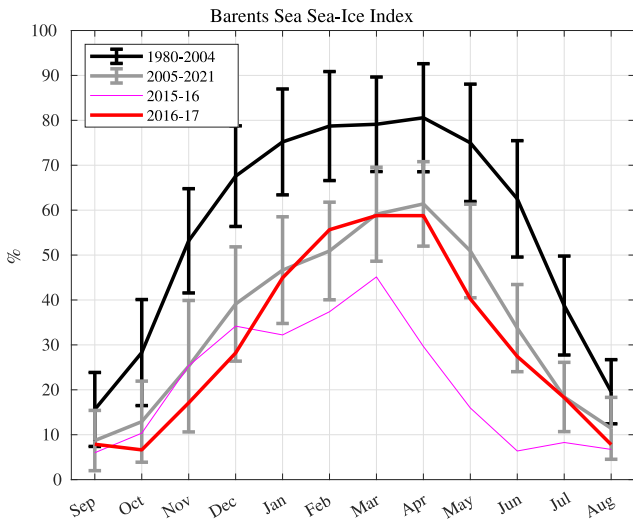
Figure 12. Barents Sea Sea-Ice Index provided by EUMETSAT-OSISAF, defined as the monthly averaged sea-ice extent between 10°E and 60°E and 72°N and 82°N. The pre- (post-)2005 climatology is shown in black (gray), respectively, jointly with the monthly standard deviation. The ice season 2016–2017 (2015–2016) is shown in red (thin magenta), respectively.

high-resolution thermal infrared imagery, exploiting the relationship between ice surface temperature and thickness, for known atmospheric energy fluxes. From 12 years of MODIS data, Preußer et al. (2015) found a winter average ice production of 28.3 km^3. Their estimates are restricted to the dark season (November–March), hence the lower values which exclude sea-ice production during spring. Finally, Rousset et al. (2015) found a somewhat lower annual ice production of 33 km^3 for the period 1999–2009 using a purely numerical approach based on the NEMO-LIM v3.6 coupled ocean-sea-ice model in a high-resolution (2 km, 75 levels) regional configuration.

From this review, the 2017 ice production of 44.2 km^3 appears as average compared with available estimates before 2011, slightly larger than the average figure of Skogseth et al. (2004) and Skogseth, Fer, and Haugan (2005), and slightly below the average estimate of Jardon et al. (2014) and Iwamoto et al. (2014), but within one standard deviation in all cases. This average ice production is in itself surprising given the brevity of the ice season in 2016–2017 that started 57 days late and lasted 152 days only compared to an average 216 days.

To appreciate the Storfjorden ice coverage from a broader perspective we display the BSSII in Figure 12. The BSSII indicates a significant recovery of regional sea-ice conditions after the strongly anomalous Winter 2015–2016 discussed by for example, Vivier et al. (2023). The maximum BSSII was 45% in 2015–2016, the smallest value since the beginning of the record in 1979, whereas it raised to 59% in 2016–2017. The return to less outstanding surface atmospheric condition during winter-spring in 2017 can further be appreciated in Figure 13 where the January through April (JFMA) average air temperature in Storfjorden was slightly cooler than the 2010–2020 average for the JFMA period, whereas it was 4°C warmer in 2016, a particularly large 4-month anomaly. However, it would be an exaggeration to describe the situation as a return to normal conditions, since the maximal BSSII value of 59% remains far from the range of values (70%–90%) before the 2005 regime shift in the northern Barents Sea (Figure 12). Indeed the Barents Sea has undergone profound changes since the mid-2000s with a reduced sea-ice import from the Arctic and an increase in salinity and temperature hampering sea ice formation (Asbjørnsen et al., 2020; Barton et al., 2018; Lind et al., 2018; Oziel et al., 2016; Schlichtholz, 2019; Skagseth et al., 2020). This regional manifestation of the so-called atlantification (Polyakov et al., 2017; Årthun et al., 2012) is particularly strong in the northwestern Barents Sea, associated with increased advection of warmer and more saline AW (Asbjørnsen et al., 2020; Schlichtholz, 2019).
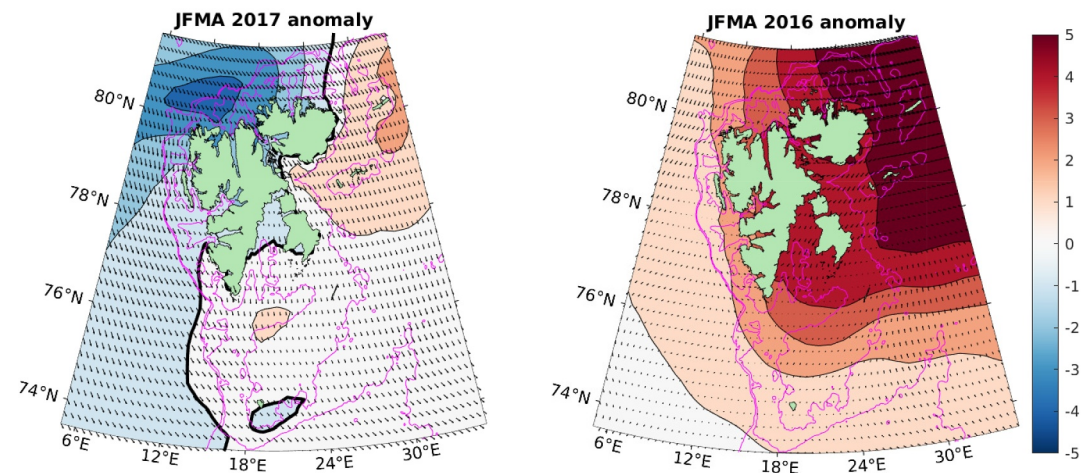

Figure 13. January-April surface air temperature (*in* °C) and wind stress anomaly relative to the period 2010–2020 for the year 2017 (left) and 2016 (right). Data are from the ERA5 reanalysis; magenta lines denote the 500, 350, and 120 m isobaths.

With a low ice coverage in the northern Barents Sea compared with the pre-2005 period and despite a two-month delay for the onset of freezing in Storfjorden, the polynya was nonetheless fairly active in 2017, producing a volume of ice in the average of previous estimates for the 1990s and 2000s. This observation, initially counter intuitive, is reminiscent of the negative winter ice growth feedback mechanism evidenced over the Arctic pack ice, whereby thinner ice grows faster than thicker ice due to an enhanced thermal conduction (Bigdeli et al., 2020; Petty et al., 2018; Stroeve et al., 2018). Here, however, in a region where ice is seasonal and production is dominated by frazil, a more likely mechanism is that a thinner, more fragile ice cover favors polynya openings and thereby frazil ice production, rather than a conductive feedback. A thinner and less abundant pack ice south of Storfjorden also hinders polynya opening to a lesser degree. This is consistent with the observed recent increase of heat release to the atmosphere in the northern Barents Sea associated with the strong ice decline (Asbjørnsen et al., 2020; Shu et al., 2021).

4.2. Dense Water Formation

CTD observations from the STEP cruise in July 2016, collected in the wake of an exceptional winter season marked by the lowest ice coverage in the Barents Sea over 40 years (Figure 12) and a strongly anomalous atmospheric warming (Figure 13, right) indicated a very unusual hydrographic situation (Vivier et al., 2023). It was characterized in particular by the absence of a gravity driven overflow of BSW at the sill barring the mouth of Storfjorden as well as its absence as a bottom plume at the exit of Storfjordrenna, where BSW was instead replaced by warmer and lighter PW ($\sigma_\theta = 27.94$ kg m^{-3}); the densest remnant BSW found in the depression of Storfjorden (at the same location as Station 17 of 2017) was relatively fresh compared with previous reports ($S = 34.95$; $\sigma_\theta = 28.12$ kg m^{-3}). Observations and analyses presented in the previous sections show a recovery of the polynya activity in 2017 with substantial dense water formation.

4.2.1. An Abundant Production Caused by a More Saline Source Water

First, examination of the properties of the BSW indicates the formation of a saline and dense specimen in 2017. At the mooring site, the densest BSW, recorded at 90 m on 10 April 2017, had a salinity of 35.74 ($\sigma_\theta = 28.79$ kg m^{-3}, Figure 5). At the bottom of the main depression (Station 17, 190 m, Figure 8a) the salinity of the remnant BSW recorded late September 2017 was lower yet quite saline with $S = 35.36$ ($\sigma_\theta = 28.47$ kg m^{-3}). It is difficult to assess whether the lower value at the depression is consistent with a dilution between the mooring location, over a 100 m depth and the depression, or whether it is owed to the delay of more than 5 months separating these measurements, allowing time for diffusing mixing with fresher water above. Whether we retain 35.74 or 35.36 as the characteristic maximum BSW salinity, the 2017 brine production was high: the historical average (1981–2002) of annual maximum salinity of BSW in Storfjorden is 35.20 ± 0.26 ($\pm$SD) according to Skogseth, Fer, and Haugan (2005).

Second, the volume of BSW produced was large with 1,318 km^3 estimated from our box model with linear stratification, which corresponds to an annual mean transport of 0.042 Sv. This value is larger than previous estimates for the period 1998–2002 (Skogseth et al., 2004; Skogseth, Fer, & Haugan, 2005) reported in Table 2, which average to 1030 ± 100 km^3 ($\pm$ SD). Part of this difference is of course methodological: this is why we also provide estimates with the regular slab-layer version of the box model. The use of a piecewise linear approximation for the surface salinity following Skogseth et al. (2004) yields V_{bsw} ranging between 1,210 and 1,540 km^3, depending on the choice for the final surface salinity, still larger than the average production estimated for the 1998–2002 epoch. Likewise, the 2017 annual mean transport of 0.042 Sv is larger than the annual mean of 0.03 Sv from 3 years (2004–2006) of moored ADCP data at the sill (Geyer et al., 2009). Only Schauer (1995) reported a larger BSW production of 1,600 km^3 (annual mean transport of 0.05 Sv) for the freezing period 1991–1992; an estimate based on mooring records 30 km south of the sill, with thus a likely additional contribution from entrainment. According to Equation 4 two factors may be responsible for the larger volume: (a) a larger sea-ice production and salt release (b) a smaller denominator $S_o - S_b$ which increases the BSW volume per unit salt rejected as noted by Skogseth et al. (2004). Regarding the first factor, the 2017 ice production of 44.2 km^3 was average as shown above (Table 3). Looking at specific years, the ice production was larger in 2000 with a volume of 44.8 km^3 but the volume of BSW formed in 2000 was 1,100 km^3, smaller than the 2017 estimate using the same method (Table 2). Likewise, the exceptional year 2002 with a sea-ice production of 60.0 km^3 produced only 1,090 km^3 of BSW according to Skogseth, Fer, and Haugan (2005). We conclude that salt rejection by sea ice

does not seem to be the main agent of the large BSW production in 2017. The most influential factor instead appears to be the initial surface salinity of 34.28 in January 2017, which was high compared with the values measured at the onset of the freezing season from 1998 to 2002 (Skogseth et al., 2004; Skogseth, Fer, & Haugan, 2005) averaging to 33.91 ± 0.30 (Table 2). A particularly outstanding figure of Table 2 is the volume transport of BSW during the production season of 0.129 Sv in 2017, which is twice as large as the average transport for the 1998–2002 epoch. This is due to the combination of a larger production and a substantially shorter freezing season of only 119 days compared with 185 days on average for 1998–2002 (Skogseth et al., 2004) or 205 days for 2003–2011 (Jardon et al., 2014). We note however that the 2017 transport is consistent with the 0.13 Sv of Schauer (1995) for a five month overflow period in 1992, a duration also shorter than the 3-year average of 180 days measured by Geyer et al. (2009). The comparison of the duration of the overflow with that of the period during which BSW is produced (freezing period) should however be made with caution since the overflow is delayed with respect to the BSW production due to the buffering effect of the 120 m sill.

4.2.2. A Dense Plume Exporting Heat Into the Deep Ocean

The large production of saline BSW in Storfjorden generated a particularly dense bottom plume in Storfjordrenna. The latter was sampled in July 2017 by three CTD sections from the AREX cruise, 45 days after the end of the freezing period. At Station 84, ~90 km downstream of the sill (Figures 7 and 8c), the cold BSW had a density of $\sigma_\theta = 28.32 \, \text{kg m}^{-3}$ ($S = 35.19$). In comparison, the maximum plume density reported by Fer et al. (2003) in June 2001 was $28.17 \, \text{kg m}^{-3}$, whereas it was about $28.27 \, \text{kg m}^{-3}$ in July-August 1986, approximately at the same location as Station 84 (Quadfasel et al., 1988, their Figure 4, Station 158). The year 1986 was an exceptional year during which the plume was observed at a depth of 2,000 m at Fram Strait. At the outlet of Storfjordrenna south of Sørkapp the bottom water density diminished to $\sigma_\theta = 28.13 \, \text{kg m}^{-3}$ ($S = 35.04$).

Consistent with the modeling works of Wobus et al. (2013) the overflow was found to split into two branches west of Sørkapp, a shallow branch continuing on the west Spitsbergen shelf and a deep branch sinking along the continental slope, tracked down to 750 m at the zonal section at 76°30′N, thus below the AW layer (Figures 8e and 8f). The deep branch appeared as a warm rather than a cold anomaly ($\sim 2°C$; Figure 8e) due to the entrainment of warm AW (Akimova et al., 2011; Quadfasel et al., 1988). The plume had a larger O_2 concentration ($\geq 290 \, \mu\text{mol kg}^{-1}$) than the ambient, its salinity (≥ 35.00) exceeded that of NSDW (34.91) and its density at the bottom reached $28.00 \, \text{kg m}^{-3}$. We note, however, that there is no report of a plume in near-bottom mooring observations collected since 2014 offshore the Spitsbergen margin over a 1040 m depth, 7 km to the south of Station 165 (Bensi et al., 2019, 2020). These authors report fluctuations in hydrography and currents peaking in winter, which they mainly attribute to topographically trapped waves excited by atmospheric forcing, although they do not exclude contributions from slope convection. This is compatible with our results since the mooring's hydrographic record is at 1020 m thus ~300 m below the maximal depth where we identify the plume's signature.

We can estimate an entrainment rate based on the observed O_2 concentration of the plume. Assuming that BSW ($[O_2] = 350 \, \mu\text{mol kg}^{-1}$ in Storfjorden) mixes with AW or MAW only ($[O_2] = 280 \, \mu\text{mol kg}^{-1}$) during its journey to the shelf break, and further assuming that O_2 is a quasi-conservative tracer at the few-month transit time scale considered here (turbulence in the bottom plume prohibits sedimentation and degradation), the volume of entrained water at the shelf break ($[O_2] = 290 \, \mu\text{mol kg}^{-1}$) is 8 times the volume of BSW exiting Storfjorden at the sill, a 700% increase. This figure is consistent with, albeit larger than previous estimates: Quadfasel et al. (1988) provided a rough estimate of 500% from the analysis of hydrographic data; the model of Jungclaus et al. (1995) lead to an entrainment rate between 200% and 600%, depending on the initial density of the BSW while the simulation of Fer and Ådlandsvik (2008) yielded ~600%; Akimova et al. (2011) came up with a 500% entrainment rate from a 1D streamtube model of the plume. We note however that our larger estimate of 700% is consistent with the fact that the BSW was particularly dense and saline in 2017: a higher density contrast causes higher entrainment (Jungclaus et al., 1995; Price & O'Neil Baringer, 1994). With our annual BSW production estimate of 0.042 Sv in 2017, this entrainment rate implies a plume transport into Fram Strait of 0.34 Sv, three times higher than the value of 0.1 Sv estimated by Quadfasel et al. (1988). However, with the presence of a shallow branch on the shelf, not all of this flux feeds the deep water layer, and this 0.34 Sv figure should be regarded as an upper bound.

The dense bottom plume in Storfjordrenna in July 2017 ($\sigma_\theta > 28.10$ kg m^{-3} at the Sørkapp Section) was in stark contrast with the weak (0.02 Sv) much lighter plume ($\sigma_\theta = 27.94$ kg m^{-3}) measured one year before at the same section (Vivier et al., 2023). However, both plumes have in common to carry relatively warm water (PW or MAW with $\theta_{\min} \geq 0$°C in 2017; PW with $\theta_{\min} \geq 1$°C in 2016). The plume was consistently substantially colder in the available literature at this location with $\theta_{\min} \leq -1.5$°C reported by Fer et al. (2003), and clearly negative values reported by Schauer (1995). The years with a documented deep reaching plume in Fram Strait are 1986, 1988, and 2002 (Akimova et al., 2011; Quadfasel et al., 1988). Hydrographic profiles are available in Storfjordrenna approximately at the Sørkapp Section in 1986 and 2002, featuring a $\theta_{\min}$ of -1°C or colder (Akimova et al., 2011, their Figure 3). These previous studies are all based on hydrographic data prior to 2005, thus before the increase in temperature and salinity in the northern Barents Sea linked to its atlantification. This suggests that the BSW overflow, which exits Storfjorden at a temperature near the freezing point, entrained and mixed with warmer water in Storfjordrenna in the post-2005 era. The analyses of Skagseth et al. (2020) and Mohamed et al. (2022) indeed show a particularly pronounced warming in Storfjordrenna. Because the entrained water is also saltier, the density of the plume remained in the historical range due to density compensation as argued by Skagseth et al. (2020) for the entire Barents Sea.

This observation raises the question of whether the formation of dense water in Storfjorden could represent a significant mechanism for exporting excess heat from the surface of the Barents Sea to the deep ocean. The corresponding annual heat storage is $\rho c_p \Delta\theta(1 + e)V_{bsw}$, where e is the entrainment rate, c_p the specific heat capacity of sea water (3,980 J kg^{-1}° K^{-1}) and $\Delta\theta$ the increase in the overflow temperature. With the 2017 values ($e = 7, V_{bsw} = 1318$ km^3), this annual heat export would be $\sim 4 \times 10^{19}$ J per degree of warming of the plume, that is a heat transport of 1.4 TW per degree. Further data are needed to robustly assess the increase in the plume temperature after 2005: the 2016–2017 observations suggest a $\Delta\theta$ of order 1°C. This additional 1.4 TW conveyed to the deep ocean is small if we compare it to the heat loss to the atmosphere in the Barents Sea (76 ± 15 TW, Smedsrud et al., 2013). However, it would be more relevant to compare this value with the changes in the various terms of the Barents Sea heat budget since the pre-2005 epoch, in order to assess whether this mechanism makes a significant contribution to absorbing the increase in the poleward heat transport by the AW. Observations do indicate a warming of the deep layer along the west Spitsbergen margin during this period. Bensi et al. (2019) analyzed the CTD data from the AREX section at 77°30′N since 1997 and found a significant long-term trend as of 2009 both in the potential temperature (0.0222°C yr^{-1}) and salinity (0.0007 yr^{-1}) of the layer below 800 m occupied by NSDW. They attribute these trends to an increase of the mixing rate between upper and deep layers caused by shelf-slope dynamics. Other processes such as changes in the Storfjorden plume properties reported here but also sediment/turbidity plumes (Fohrmann et al., 1998; Kämpf et al., 1999) may have contributed to this warming and slight salinification since 2009.

This mechanism of heat storage at depth, underneath the AW layer, is viable as long as the high density of the BSW is maintained, which requires a vivid polynya. The generation of a lighter overflow, as in 2016, could instead contribute to warm the halocline layer, with likely consequences on sea-ice melt. Timmermans et al. (2018) showed for instance that the warming of the Beaufort Gyre halocline was caused by the subduction of warmer surface water from the basin margins (northern Chukchi Sea). At a regional scale, the warming of the intermediate and surface water (the Arctic Water) in the Spitsbergen Polar Current/South Cape Current could impact shelf-fjord water exchange and the sea ice conditions in the West Spitsbergen fjords, as reported for Isfjorden (Skogseth et al., 2020) and Kongsfjorden (Tverberg et al., 2019).

5. Summary and Concluding Remarks

One year of mooring observations in Storfjorden together with a network of CTD sections in Storfjorden and Storfjordrenna provided a comprehensive description of the formation of BSW in the Storfjorden polynya during Winter 2016–2017 and the subsequent evolution of the Storfjorden overflow down to the western shelf break and slope of Svalbard. The ice production during the freezing season 2016–2017 was estimated with the model of Jardon et al. (2014) forced by ERA5 atmospheric products and nudged to AMSR2 daily satellite SIC data. A simple salinity budget model was developed to estimate the volume of BSW forming in Storfjorden. This model builds on previous slab-layer box model approaches, assuming instead a linear salinity profile in the water column; it is forced with the estimated salt release from sea ice and with the water column salt content determined from the mooring observations.

These observations and analyses indicate a vigorous recovery of the BSW formation in Storfjorden polynya in 2017 after the report of an unusual hydrographic state in July 2016 (Vivier et al., 2023), characterized in particular by the absence of a BSW overflow at the sill, a relatively fresh remnant BSW in Storfjorden (S_{max} = 34.95), and a weak bottom plume exiting Storfjordrenna, carrying light PW (σ_θ = 27.94 kg m^{-3}). In 2017, mooring observations show instead the formation of a saline specimen of BSW (S_{max} = 35.74), although sea ice first appeared in Storfjorden with a nearly two month delay after a particularly warm autumn in Svalbard: The 2016–2017 ice season lasted only 152 days instead of 216 days on average. In spite of the shortened freezing season 44.2 km^3 of sea ice were formed, releasing 1.13 Gt of salt in the ocean according to the polynya model. These values are in the average of previous estimates pertaining to the 1990s and 2000s, which may seem surprising since the sea-ice cover in the northern Barents Sea has substantially declined since the mid 2000s with its atlantification (e.g., Lind et al., 2018). The maximum BSSII ranged between 70% and 90% before the 2005 regime shift as opposed to 59% in 2016–2017. Analogous to the negative conductive feedback of sea ice growth evidenced over the Arctic pack ice (e.g., Petty et al., 2018), the mechanism of sustained ice formation is more likely that a thinner, more fragile ice favors polynya openings and frazil ice production. This mechanism seems to hold up to a certain point, however, and other factors come also into play. In 2015–2016 the BSSII hit its 40 year record low of 45% but the brine production was weak as can be judged from the low salinity of the BSW sampled in July 2016: Winter-Spring 2016 was anomalously warm while Winter-Spring 2017 presented average atmospheric conditions for the season (Figure 13).

The volume of BSW produced in 2017, estimated from our box model with linear stratification, was 1,318 km^3, corresponding to an annual mean transport of 0.042 Sv. This production is larger than previous estimates of 1030 ± 100 km^3 (± SD) for the period 1998–2002 (Skogseth, Fer, & Haugan, 2005), even when accounting for methodological differences. The larger volume of BSW produced in 2017 is not caused by a larger ice production in the polynya, which was average, but instead appears to be associated with a more saline source water (here ArW): the initial surface salinity of 34.28 at the onset of freezing was 0.37 larger than the 1998–2002 average. The preconditioning of Storfjorden with a more saline water is consistent with the overall increase in water temperature and salinity in the northern Barents Sea since 2005 (e.g., Lind et al., 2018). The same holds true in summer: SSW once described as the most abundant water mass in the upper 60 m of Storfjorden in summer (Haarpaintner, O'Dwyer, et al., 2001; Skogseth, Haugan, & Jakobsson, 2005) was absent in the July 2016 survey and nearly absent from our 2016–2017 observations for the second year in a row. It was replaced by a saltier water mass, exceeding the 34.4 threshold. This change in hydrographic characteristics suggests to revise the definition of SSW and extend its salinity range to 34.8 rather than 34.4 ($1 < \theta \leq 3°C$; $S < 34.8$). We also note an intrusion of water of Atlantic origin (MAW, PW) into Storfjorden, north of the sill, for the second summer in a row. However the intrusion was limited to the southern part of Storfjorden in September 2017, and was far less massive than the July 2016 flooding reported up to 78°N (Vivier et al., 2023). Bursts of MAW were identified at the mooring (78°N) through Summer-Fall 2016, below 50 m (Figure 5).

The high production of saline BSW in Storfjorden generated a dense overflow sampled in July 2017 from CTD Sections in Storfjordrenna as well as on the shelf break and slope west of Sørkapp. The plume was found to split at the shelf break with a shallow branch continuing on the shelf and a main branch sinking along the continental slope, consistent with the modeling of Wobus et al. (2013). The deep branch was tracked down to 750 m at the section west of Sørkapp, thus entering the NSDW layer below the AW layer (Figures 8e and 8f). We estimate an entrainment rate of 700% based on the plume O_2 concentration, larger but consistent with previous estimates. This entrainment rate implies a plume transport of 0.34 Sv into Fram Strait, three times larger than that estimated by Quadfasel et al. (1988), which was based on a particularly low value for the BSW production. This is an upper bound, however, as part of this flux is diverted into the shallow branch.

Although much denser in 2017 ($\sigma_\theta > 28.10$ kg m^{-3}) than in 2016 ($\sigma_\theta = 27.94$ kg m^{-3}), the 2017 overflow at the exit of Storfjordrenna was nevertheless also warm ($\theta_{min} \geq 0°C$), substantially warmer than their pre-2005 counterparts (see e.g., Akimova et al., 2011; Fer et al., 2003), on the order of one degree. This difference is owed to the entrainment of a warmer water in Storfjordrenna since the BSW overflow exits Storfjorden close to the freezing point. Storfjordrenna is indeed an area of the Barents Sea that has particularly warmed since 2005 (Mohamed et al., 2022; Skagseth et al., 2020). The observation of a warmer overflow suggests that a part of the excess surface heat of the Barents Sea could be entering the deep layer of the Arctic and Nordic Seas through this process. The deep layer along the western margin of Spitsbergen has indeed warmed since 2009 (Bensi

et al., 2019). An upper bound for the additional heat export relative to the pre-2005 values is 1.4 TW or $\sim 4 \times 10^{19}$ J per year, based on the 2017 BSW production.

A question that remains to be addressed is whether the 2017 insertion of a warmer plume underneath the AW layer was a one of kind event, owed to the particularly saline BSW formed in 2017 that permitted a density compensation or, instead, as found by Skagseth et al. (2020) the increasing salinity in the northern Barents Sea compensates for the warming leaving the outflow densities relatively unperturbed. While the warming trend in Storfjordrenna is clearly apparent (Lind et al., 2018; Mohamed et al., 2022; Skagseth et al., 2020), the freshwater content does not seem to have reduced as much there as elsewhere in the northern Barents Sea (Lind et al., 2018, their Figure 3). This question may be merely rhetorical, however, if the Storfjorden polynya consistently produces a more saline BSW in a warmer and saltier Barents Sea. Our analyses indicate that the large production of saline BSW in 2017, was influenced by the preconditioning of Storfjorden with a more saline source water whereas the ice production was average. On the contrary the deep plume observed into Fram Strait in 2002 (Akimova et al., 2011) was clearly associated with an outstanding ice production of 60 km^3 (Skogseth, Fer, & Haugan, 2005). This point requires longer series to be addressed.

Overall our results suggest that dense water formation in the Storfjorden polynya may not, at least for now, be hampered by the atlantification of the Barents Sea, and perhaps even temporarily favored. Despite a shorter freezing season, the ice production and salt release remained average, while preconditioning with a saltier source water permitted the production of a particularly saline BSW in large volumes. This is consistent with the report of a denser Barents Sea Water for the post 2005 period (Barton et al., 2018). The situation may of course change radically if an excessive warming prevents sea-ice formation thus threatening the very existence of a polynya: the Barents Sea could become ice-free in winter within a few decades, although there is a large spread in climate model projections (Onarheim & Årthun, 2017). But even before such an extreme situation, the outstanding year 2016 could be a prefiguration of the future of the polynya (Vivier et al., 2023). The year 2016 was exceptional: the heat content of the upper 100 m of the northern Barents Sea exceeded the 1970–1999 mean by 6.3 standard deviations (Lind et al., 2018). In Storfjorden the strongly anomalous atmospheric warming during the winter-spring (Figure 13) limited brine release and a warm and light plume, unable to sink under the AW layer, was instead found at the exit of Storfjordrenna. In this case the Storfjorden polynya may ultimately contribute to warm the cold halocline layer in the Arctic, as found for example, in the Beaufort Gyre (Timmermans et al., 2018), rather than storing heat in the deep ocean. Longer series of observations are needed to assess which will be the pathway of the Storfjorden polynya. Although the 2017 scenario, where part of the excess heat is exported in the deep ocean is clearly less threatening for the Arctic ice cover, it may not be without consequences either since the intermediate and deep waters of the Arctic and Norwegian-Greenland Seas ultimately feed the Atlantic meridional overturning circulation (Lozier et al., 2019).

Data Availability Statement

Hydrographic and velocity data from the mooring (Vivier et al., 2019) are available at the French oceanographic data center SEANOE at https://www.seanoe.org/data/00515/62632/; AREX 2017 selected hydrographic profiles (Goszczko, 2024) are available on Zenodo at https://doi.org/10.5281/zenodo.11088177.

References

Aagaard, K. (1981). On the deep circulation in the Arctic Ocean. *Deep-Sea Research, Part A: Oceanographic Research Papers*, *28*(3), 251–268. https://doi.org/10.1016/0198-0149(81)90066-2

Aagaard, K., Coachman, L., & Carmack, E. (1981). On the halocline of the Arctic Ocean. *Deep-Sea Research, Part A*, *28*(6), 529–545. https://doi.org/10.1016/0198-0149(81)90115-1

Aagaard, K., Swift, J. H., & Carmack, E. C. (1985). Thermohaline circulation in the Arctic Mediterranean seas. *Journal of Geophysical Research*, *90*(C3), 4833–4846. https://doi.org/10.1029/JC090iC03p04833

Akimova, A., Schauer, U., Danilov, S., & Núñez-Riboni, I. (2011). The role of the deep mixing in the Storfjorden shelf water plume. *Deep Sea Research Part I: Oceanographic Research Papers*, *58*(4), 403–414. https://doi.org/10.1016/j.dsr.2011.02.001

Anderson, L. G., Falck, E., Jones, E. P., Jutterstrom, S., & Swift, J. H. (2004). Enhanced uptake of atmospheric CO_2 during freezing of seawater: A field study in Storfjorden, Svalbard. *Journal of Geophysical Research: Oceans*, *109*, C06004. https://doi.org/10.1029/2003JC002120

Anderson, L. G., Peter Jones, E., Lindegren, R., Rudels, B., & Sehlstedt, P.-I. (1988). Nutrient regeneration in cold, high salinity bottom water of the Arctic shelves. *Continental Shelf Research*, *8*(12), 1345–1355. https://doi.org/10.1016/0278-4343(88)90044-1

Årthun, M., Eldevik, T., Smedsrud, L. H., Skagseth, Ø., & Ingvaldsen, R. (2012). Quantifying the influence of Atlantic heat on Barents Sea ice variability and retreat. *Journal of Climate*, *25*(13), 4736–4743. https://doi.org/10.1175/JCLI-D-11-00466.1

Asbjørnsen, H., Årthun, M., Skagseth, O., & Eldevik, T. (2020). Mechanisms underlying recent Arctic atlantification. *Geophysical Research Letters*, *47*(15), e2020GL088036. https://doi.org/10.1029/2020GL088036

Barton, B. I., Lenn, Y.-D., & Lique, C. (2018). Observed Atlantification of the Barents Sea causes the Polar Front to limit the expansion of winter sea ice. *Journal of Physical Oceanography*, *48*(8), 1849–1866. https://doi.org/10.1175/JPO-D-18-0003.1

Bensi, M., Kovačević, V., Langone, L., Aliani, S., Ursella, L., Goszczko, I., et al. (2019). Deep flow variability offshore south-west Svalbard (Fram Strait). *Water*, *11*(4), 683. https://doi.org/10.3390/w11040683

Bensi, M., Kovačević, V., Langone, L., Miserocchi, S., Demarte, M., & Ivaldi, R. (2020). Spitsbergen oceanic and atmospheric interactions. In *SESS report 2019—The state of Environmental science in Svalbard—An annual report* (pp. 250–261). Svalbard Integrated Arctic Earth Observing System. https://doi.org/10.5281/zenodo.4777750

Bigdeli, A., Nguyen, A. T., Pillar, H. R., Ocaña, V., & Heimbach, P. (2020). Atmospheric warming drives growth in arctic sea ice: A key role for snow. *Geophysical Research Letters*, *47*(20), e2020GL090236. https://doi.org/10.1029/2020GL090236

Cavalieri, D., & Martin, S. (1994). The contributions of Alaskan, Siberian, and Canadian coastal polynyas to the cold halocline layer of the Arctic Ocean. *Journal of Geophysical Research*, *99*(C9), 18343–18362. https://doi.org/10.1029/94JC01169

Edson, J. B., Jampana, V., Weller, R. A., Bigorre, S. P., Plueddemann, A. J., Fairall, C. W., et al. (2013). On the exchange of momentum over the open ocean. *Journal of Physical Oceanography*, *43*(8), 1589–1610. https://doi.org/10.1175/JPO-D-12-0173.1

Fairall, C., Bradley, E., Hare, J., Grechev, A., & Edson, J. (2003). Bulk parameterization of air-sea fluxes: Updates and verification for the COARE algorithm. *Journal of Climate*, *4*, 571–591. https://doi.org/10.1175/1520-0442(2003)016<0571:bpoasf>2.0.co;2

Fer, I., & Ådlandsvik, B. (2008). Descent and mixing of the overflow plume from Storfjord in Svalbard: An idealized numerical model study. *Ocean Science*, *4*(2), 115–132. https://doi.org/10.5194/os-4-115-2008

Fer, I., Skogseth, R., & Jaccard, P. (2003). Observations of the Storfjorden overflow. *Deep-Sea Research*, *50*, 1283–1303. https://doi.org/10.1016/S0967-0637(03)00124-9

Fohrmann, H., Backhaus, J. O., Blaume, F., & Rumohr, J. (1998). Sediments in bottom-arrested gravity plumes: Numerical case studies. *Journal of Physical Oceanography*, *28*(11), 2250–2274. https://doi.org/10.1175/1520-0485(1998)028<2250:SIBAGP>2.0.CO;2

Geyer, F., Fer, I., & Eldevik, T. (2009). Dense overflow from an Arctic fjord: Mean seasonal cycle, variability and wind influence. *Continental Shelf Research*, *29*(17), 2110–2121. https://doi.org/10.1016/j.csr.2009.08.003

Goszczko, I. (2024). AREX 2017 selected hydrographic profiles: CTD and oxygen concentration in the south-west Spitsbergen area [Dataset]. *Zenodo*. https://doi.org/10.5281/zenodo.11088177

Haarpaintner, J. (1999). The Storfjorden polynya: ERS-2 SAR observations and overview. *Polar Research*, *18*(2), 175–182. https://doi.org/10.1111/j.1751-8369.1999.tb00290.x

Haarpaintner, J., Gascard, J.-C., & Haugan, P. M. (2001). Ice production and brine formation in Storfjorden, Svalbard. *Journal of Geophysical Research*, *106*(C7), 1–13. https://doi.org/10.1029/1999JC000133

Haarpaintner, J., Haugan, P. M., & Gascard, J.-C. (2001). Interannual variability of the Storfjorden (Svalbard) ice cover and ice production observed by ERS-2 SAR. *Annals of Glaciology*, *33*, 430–436. https://doi.org/10.3189/172756401781818392

Haarpaintner, J., O'Dwyer, J., Gascard, J.-C., Haugan, P. M., Schauer, U., & Østerhus, S. (2001). Seasonal transformation of water masses, circulation and brine formation observed in Storfjorden, Svalbard. *Annals of Glaciology*, *33*, 437–443. https://doi.org/10.3189/172756401781818635

Hersbach, H., Bell, B., Berrisford, P., Hirahara, S., Horányi, A., Muñoz-Sabater, J., et al. (2020). The ERA5 global reanalysis. *Quarterly Journal of the Royal Meteorological Society*, *146*(730), 1999–2049. https://doi.org/10.1002/qj.3803

Iwamoto, K., Ohshima, K. I., & Tamura, T. (2014). Improved mapping of sea ice production in the Arctic Ocean using AMSR-E thin ice thickness algorithm. *Journal of Geophysical Research*, *119*(6), 3574–3594. https://doi.org/10.1002/2013JC009749

Jardon, F. P., Vivier, F., Bouruet-Aubertot, P., Lourenço, A., Cuypers, Y., & Willmes, S. (2014). Ice production in Storfjorden (Svalbard) estimated from a model based on AMSR-E observations: Impact on water mass properties. *Journal of Geophysical Research: Oceans*, *119*(1), 377–393. https://doi.org/10.1002/2013JC009322

Jungclaus, J. H., Backhaus, J. O., & Fohrmann, H. (1995). Outflow of dense water from the Storfjord in Svalbard: A numerical model study. *Journal of Geophysical Research*, *100*(C12), 24719–24728. https://doi.org/10.1029/95JC02357

Kämpf, J., Backhaus, J. O., & Fohrmann, H. (1999). Sediment-induced slope convection: Two-dimensional numerical case studies. *Journal of Geophysical Research*, *104*(C9), 20509–20522. https://doi.org/10.1029/1999JC900157

Langehaug, H. R., & Falck, E. (2012). Changes in the properties and distribution of the intermediate and deep waters in the Fram Strait. *Progress in Oceanography*, *96*(1), 57–76. https://doi.org/10.1016/j.pocean.2011.10.002

Lilly, J. M. (2021). jLab: A data analysis package for Matlab, v. 1.7.1. https://doi.org/10.5281/zenodo.4547006

Lind, S., Ingvaldsen, R., & Furevik, T. (2018). Arctic warming hotspot in the northern Barents Sea linked to declining sea-ice import. *Nature Climate Change*, *8*(7), 634–639. https://doi.org/10.1038/s41558-018-0205-y

Loeng, H. (1991). Features of the physical oceanographic conditions of the Barents Sea. *Polar Research*, *10*(1), 5–18. https://doi.org/10.1111/j.1751-8369.1991.tb00630.x

Lozier, M. S., Li, F., Bacon, S., Bahr, F., Bower, A. S., Cunningham, S. A., et al. (2019). A sea change in our view of overturning in the subpolar North Atlantic. *Science*, *363*(6426), 516–521. https://doi.org/10.1126/science.aau6592

Martin, S., Drucker, R., Kwok, R., & Holt, B. (2004). Estimation of the thin ice thickness and heat flux for the Chukchi Sea Alaskan coast polynya from special sensor microwave/imager data, 1990–2001. *Journal of Geophysical Research*, *109*(C10), 1757. https://doi.org/10.1029/2004JC002428

Martin, S., & Kauffman, P. (1981). A field and laboratory study of wave damping by grease ice. *Journal of Glaciology*, *27*(96), 283–313. https://doi.org/10.3189/S0022143000015392

Maykut, G. A. (1986). The surface heat and mass balance. In N. Untersteiner (Ed.), *The geophysics of sea ice, chapter 5* (pp. 395–465). Plenum.

McDougall, T. J., & Barker, P. M. (2011). Getting started with TEOS-10 and the Gibbs seawater (GSW) oceanographic toolbox, 28 pp., SCOR/IAPSO WG127.

Midttun, L. (1985). Formation of dense bottom water in the Barents Sea. *Deep-Sea Research, Part A: Oceanographic Research Papers*, *32*(10), 1233–1241. https://doi.org/10.1016/0198-0149(85)90006-8

Mohamed, B., Nilsen, F., & Skogseth, R. (2022). Marine heatwaves characteristics in the Barents Sea based on high resolution satellite data (1982–2020). *Frontiers in Marine Science*, *9*, 821646. https://doi.org/10.3389/fmars.2022.821646

Morales Maqueda, M. A., Willmott, A. J., & Biggs, N. R. T. (2004). Polynya dynamics: A review of observation and modelling. *Review of Geophysics*, *42*(1), RG1004. https://doi.org/10.1029/2002RG000116

Onarheim, I. H., & Årthun, M. (2017). Toward an ice-free Barents Sea. *Geophysical Research Letters*, *44*(16), 8387–8395. https://doi.org/10.1002/2017GL074304

Oziel, L., Sirven, J., & Gascard, J.-C. (2016). The Barents Sea frontal zones and water masses variability (1980–2011). *Ocean Science*, *12*(1), 169–184. https://doi.org/10.5194/os-12-169-2016

Pawlowicz, R. (2020). M_map: A mapping package for Matlab [Computer Software]. *Computer Software*. www.eoas.ubc.ca/~rich/map.html

Petty, A. A., Holland, M. M., Bailey, D. A., & Kurtz, N. T. (2018). Warm Arctic, increased winter sea ice growth? *Geophysical Research Letters*, *45*(23), 12922–12930. https://doi.org/10.1029/2018GL079223

Polyakov, I. V., Pnyushkov, A. V., Alkire, M. B., Ashik, I. M., Baumann, T. M., Carmack, E. C., et al. (2017). Greater role for atlantic inflows on sea-ice loss in the Eurasian basin of the Arctic Ocean. *Science*, *356*(6335), 285–291. https://doi.org/10.1126/science.aai8204

Preußer, A., Willmes, S., Heinemann, G., & Paul, S. (2015). Thin-ice dynamics and ice production in the Storfjorden polynya for winter seasons 2002/2003–2013/2014 using MODIS thermal infrared imagery. *The Cryosphere*, *9*(3), 1063–1073. https://doi.org/10.5194/tc-9-1063-2015

Price, J. F., & O'Neil Baringer, M. (1994). Outflows and deep water production by marginal seas. *Progress in Oceanography*, *33*(3), 161–200. https://doi.org/10.1016/0079-6611(94)90027-2

Quadfasel, D., Rudels, B., & Kurz, K. (1988). Outflow of dense water from a Svalbard fjord into the Fram Strait. *Deep-Sea Research, Part A: Oceanographic Research Papers*, *35*(7), 1143–1150. https://doi.org/10.1016/0198-0149(88)90006-4

Rousset, C., Vancoppenolle, M., Madec, G., Fichefet, T., Flavoni, S., Barthélemy, A., et al. (2015). The Louvain-La-Neuve sea-ice model LIM3.6: Global and regional capabilities. *Geoscientific Model Development. Special Issue: Nucleus for European Modelling of the Ocean NEMO*, *8*(10), 2991–3005. https://doi.org/10.5194/gmd-8-2991-2015

Rudels, B. (1986). The θ-S relations in the northern seas: Implications for the deep circulation. *Polar Research*, *4*(2), 133–159. https://doi.org/10.1111/j.1751-8369.1986.tb00527.x

Rudels, B., Björk, G., Nilsson, J., Winsor, P., Lake, I., & Nohr, C. (2005). The interaction between waters from the Arctic Ocean and the Nordic seas north of Fram Strait and along the East Greenland current: Results from the Arctic Ocean-02 Oden expedition. *Journal of Marine Systems*, *55*(1), 1–30. https://doi.org/10.1016/j.jmarsys.2004.06.008

Rudels, B., & Quadfasel, D. (1991). Convection and deep water formation in the Arctic Ocean-Greenland sea system. *Journal of Marine Systems*, *2*(3), 435–450. https://doi.org/10.1016/0924-7963(91)90045-V

Schauer, U. (1995). The release of brine-enriched shelf water from Storfjord into the Norwegian Sea. *Journal of Geophysical Research*, *100*(C8), 16015–16028. https://doi.org/10.1029/95JC01184

Schlichtholz, P. (2019). Subsurface ocean flywheel of coupled climate variability in the Barents Sea hotspot of global warming. *Scientific Reports*, *9*(1), 13692. https://doi.org/10.1038/s41598-019-49965-6

Schlichtholz, P., & Houssais, M.-N. (1999). An inverse modeling study in Fram Strait. Part II: Water mass distribution and transports. *Deep Sea Research Part II: Topical Studies in Oceanography*, *46*(6), 1137–1168. https://doi.org/10.1016/S0967-0645(99)00017-X

Shu, Q., Wang, Q., Song, Z., & Qiao, F. (2021). The poleward enhanced Arctic Ocean cooling machine in a warming climate. *Nature Communications*, *12*(1), 2966. https://doi.org/10.1038/s41467-021-23321-7

Skagseth, Ø., Eldevik, T., Årthun, M., Asbjørnsen, H., Lien, V. S., & Smedsrud, L.-H. (2020). Reduced efficiency of the Barents Sea cooling machine. *Nature Climate Change*, *10*(7), 661–666. https://doi.org/10.1038/s41558-020-0772-6

Skogseth, R., Fer, I., & Haugan, P. M. (2005). Dense-water production and overflow from an Arctic coastal polynya in Storfjorden. In H. Drange, T. Dokken, T. Furevik, R. Gerdes, & W. Berger (Eds.), *The Nordic seas: An integrated perspective-oceanography, climatology, biogeochemistry, and modeling*. American Geophysical Union. https://doi.org/10.1029/158GM07

Skogseth, R., Haugan, P., & Haarpaintner, J. (2004). Ice and brine production in Storfjorden from four winters of satellite and in situ observations and modeling. *Journal of Geophysical Research*, *109*, C10008. https://doi.org/10.1029/2004JC002384

Skogseth, R., Haugan, P. M., & Jakobsson, M. (2005). Watermass transformations in Storfjorden. *Continental Shelf Research*, *25*(5), 667–695. https://doi.org/10.1016/j.csr.2004.10.005

Skogseth, R., McPhee, M. G., Nilsen, F., & Smedsrud, L. H. (2013). Creation and tidal advection of a cold salinity front in Storfjorden: 1. Polynya dynamics. *Journal of Geophysical Research*, *118*(7), 3278–3291. https://doi.org/10.1002/jgrc.20231

Skogseth, R., Olivier, L., Nilsen, F., Falck, E., Fraser, N., Tverberg, V., et al. (2020). Variability and decadal trends in the Isfjorden (Svalbard) ocean climate and circulation—An indicator for climate change in the European arctic. *Progress in Oceanography*, *187*, 102394. https://doi.org/10.1016/j.pocean.2020.102394

Skogseth, R., Smedsrud, L. H., Nilsen, F., & Fer, I. (2008). Observations of hydrography and downflow of brine-enriched shelf water in the Storfjorden polynya, Svalbard. *Journal of Geophysical Research*, *113*(C8), C08049. https://doi.org/10.1029/2007JC004452

Smedsrud, L. H., Esau, I., Ingvaldsen, R. B., Eldevik, T., Haugan, P. M., Li, C., et al. (2013). The role of the Barents Sea in the Arctic climate system. *Reviews of Geophysics*, *51*(3), 415–449. https://doi.org/10.1002/rog.20017

Spreen, G., Kaleschke, L., & Heygster, G. (2008). Sea ice remote sensing using AMSR-E 89 Ghz channels. *Journal of Geophysical Research*, *113*(C2), C02S03. https://doi.org/10.1029/2005JC003384

Stroeve, J. C., Schroder, D., Tsamados, M., & Feltham, D. (2018). Warm winter, thin ice? *The Cryosphere*, *12*(5), 1791–1809. https://doi.org/10.5194/tc-12-1791-2018

Swift, J. H., Takahashi, T., & Livingston, H. D. (1983). The contribution of the Greenland and Barents seas to the deep water of the Arctic Ocean. *Journal of Geophysical Research*, *88*(C10), 5981–5986. https://doi.org/10.1029/JC088iC10p05981

Tamura, T., & Ohshima, K. I. (2011). Mapping of sea ice production in the arctic coastal polynyas. *Journal of Geophysical Research*, *116*(C7), C07030. https://doi.org/10.1029/2010JC006586

Timmermans, M.-L., Toole, J., & Krishfield, R. (2018). Warming of the interior Arctic Ocean linked to sea ice losses at the basin margins. *Science Advances*, *4*(8), eaat6773. https://doi.org/10.1126/sciadv.aat6773

Tverberg, V., Skogseth, R., Cottier, F., Sundfjord, A., Walczowski, W., Inall, M., et al. (2019). The Kongsfjorden transect: Seasonal and inter-annual variability in hydrography. In H. Hop & C. Weincke (Eds.), *The ecosystem of Kongsfjorden*.

Vivier, F., Lourenço, A., Michel, E., & Pruchon, A. (2019). Hydrography and currents in Storfjorden (Svalbard) from the STEP 2016–2017 moorings [Dataset]. *SEANOE*. https://doi.org/10.17882/62632

Vivier, F., Lourenço, A., Michel, E., Skogseth, R., Rousset, C., Lansard, B., et al. (2023). Summer hydrography and circulation in Storfjorden, Svalbard, following a record low winter Sea-Ice extent in the Barents Sea. *Journal of Geophysical Research: Oceans*, *128*(2), e2022JC018648. https://doi.org/10.1029/2022JC018648

Walczowski, W., Beszczynska-Möller, A., Wieczorek, P., Merchel, M., & Grynczel, A. (2017). Oceanographic observations in the Nordic sea and Fram Strait in 2016 under the IO PAN long-term monitoring program AREX. *Oceanologia*, *59*(2), 187–194. https://doi.org/10.1016/j.oceano.2016.12.003

Winsor, P., & Björk, G. (2000). Polynya activity in the Arctic Ocean from 1958 to 1997. *Journal of Geophysical Research*, *105*(C4), 8789–8803. https://doi.org/10.1029/1999JC900305

Wobus, F., Shapiro, G. I., Huthnance, J. M., Maqueda, M. A. M., & Aksenov, Y. (2013). Tidally induced lateral dispersion of the Storfjorden overflow plume. *Ocean Science*, *9*(5), 885–899. https://doi.org/10.5194/os-9-885-2013

References From the Supporting Information

Kundu, P. K., Blanton, J. O., & Janopaul, M. M. (1981). Analysis of current observations on the Georgia shelf. *Journal of Physical Oceanography*, *11*(8), 1139–1149. https://doi.org/10.1175/1520-0485(1981)011⟨1139:AOCOOT⟩2.0.CO;2